LOW ORDER MODELS FOR HYBRID GAS BEARINGS

by

NICHOLAS SAVOULIDES

Bachelor of Science in Aeronautics and Astronautics
Massachusetts Institute of Technology, 1998

Submitted to the Department of Aeronautics and Astronautics
in partial fulfillment of the requirements for the degree of

MASTER OF SCIENCE IN AERONAUTICS AND ASTRONAUTICS

at the

MASSACHUSETTS INSTITUTE OF TECHNOLOGY

February 2000

Author:_____

Department of Aeronautics and Astronautics
December 22, 1999

Certified by:_____

Kenneth S. Breuer
Visiting Associate Professor of Aeronautics and Astronautics
Thesis Supervisor

Accepted by:_____

Nesbitt W. Hagood
Associate Professor of Aeronautics and Astronautics
Chairman, Departmental Graduate Committee

LOW ORDER MODELS FOR HYBRID GAS BEARINGS

by

NICHOLAS SAVOULIDES

Submitted to the Department of Aeronautics and Astronautics
on December, 1999 in partial fulfillment of the requirements for the degree of
Master of Science in Aeronautics and Astronautics

ABSTRACT

A low order model was created to analyze a small scale gas bearing designed for the MIT microfabricated gas turbine engine. The journal has a diameter of 4.1 mm and is designed to spin at 2 million rpm. Due to microfabrication constraints, the bearing will have a very low length to diameter ratio (O(.1)) and a very large clearance to radius ratio (O(0.01)). As a result, the bearing lies outside the standard operating regime and stable operation is a challenge. The model presented in this paper is able to predict the bearing's behavior under hydrodynamic, hydrostatic and hybrid operation. The model is an application of Newton's second law of motion to the journal, after it has undergone a sudden perturbation from an assumed stable operating point. The equations include stiffness coefficients taken from a numerical simulation of the compressible Reynolds equation, and damping coefficients taken from a short width Full-Sommerfeld solution. The equations of motion are then modified, and rewritten in matrix form using variables relevant to the bearing literature. By studying the eigenvalues of the linear model, it is possible to determine at any operating point: 1) whether the journal can sustain stable operation, and 2) the whirling frequency of the journal. The model's results have been validated for hydrodynamic operation based on the Half-Sommerfeld and Full-Sommerfeld model coefficients.

Analysis shows that the best way to operate the bearing is in a hybrid mode where the bearing relies on hydrostatics at low speeds and hydrodynamics at high speeds. However, in transitioning from hydrostatic to hydrodynamic operation, the model shows that the bearing is prone to instability problems and great care must be taken in the operating schedule.

Thesis Supervisor: Kenneth S. Breuer
Title: Visiting Associate Professor of Aeronautics and Astronautics

AKNOWLEDGEMENTS

First and foremost, I would like to thank Professor Kenneth S. Breuer for all his help, enthusiasm, and understanding during times of difficulty. It was a true pleasure working with him, in all respects!

I would also like to thank the rest of the faculty members and students that were involved in the Microengine Project, making special note of Professor Alan Epstein who has managed to remarkably coordinate such a large team; also Professor John Brisson, Dr Fredric Ehrich, Dr Stuart Jacobson, Luc Frechette, D.J. Orr, Ed Piekos, Chris Protz, Jon Protz, and Chee Wei Wong who have always been very friendly and willing to help.

I would also like to thank my parents and relatives whose support has been immense. They have always been there for me, believing in my abilities, and always providing lots of motivation.

Finally, I would like to mention that I am extremely grateful to the Rolls Royce Company, through which I was granted the Sir Frank Whittle Fellowship Award.

TABLE OF CONTENTS

LIST OF FIGURES

LIST OF TABLES

LIST OF VARIABLES

c	*journal (rotor) -bearing clearance*
L	*journal (rotor) length*
m	*journal (rotor) mass*
r	*journal (rotor) radius*
$\psi = c/r$	*ratio*
$\lambda = 2r/L$	*ratio*
e	*eccentricity*
$\varepsilon = e/c$	*eccentricity ratio*
Φ	*attitude angle*
x	*journal (rotor) center x-axis location*
z	*journal (rotor) center z-axis location*
$x_{new} = x/c$	*dimensionless journal (rotor) center x-axis location*
$z_{new} = z/c$	*dimensionless journal (rotor) center z-axis location*
Δx	*journal (rotor) perturbation displacement in x-direction*
Δz	*journal (rotor) perturbation displacement in z-direction*
t	*time*
$\tau = t\omega$	*dimensionless time*
$\Delta\dot{x} = \frac{d(\Delta x)}{dt}$	*journal (rotor) perturbation velocity in x-direction*
$\Delta\dot{z} = \frac{d(\Delta z)}{dt}$	*journal (rotor) perturbation velocity in z-direction*
$\Delta\ddot{x} = \frac{d^2(\Delta x)}{dt^2}$	*journal (rotor) perturbation acceleration in x-direction*
$\Delta\ddot{z} = \frac{d^2(\Delta z)}{dt^2}$	*journal (rotor) perturbation acceleration in z-direction*
w_r	*externally applied load force*
w_x	*internal reaction force in x-direction*
w_z	*internal reaction force in z-direction*
Utip	*journal (rotor) tip speed*
ω	*journal (rotor) angular rotational speed*
ω_n	*journal (rotor) natural frequency associated only with hydrostatics*
ω_{whirl}	*journal (rotor) whirl frequency*

A_h	*surface area over which high pressure plenum is acting on the journal*
A_l	*surface area over which low pressure plenum is acting on the journal*
μ	*viscosity*
P_a	*"ambient pressure" surrounding the journal (rotor)*
P_{add}	*start-up assist pressure*
P_{atm}	*atmospheric pressure*
P_{int}	*turbine inter-row pressure*
P_{main}	*main turbine air pressure*
P_{PH}	*high pressure plenum pressure*
P_{PL}	*low pressure plenum pressure*
P_{supply}	*pressure supplied to the restrictor*
ΔP	*weighted axial pressure difference across the journal (rotor)*
$\Delta P_{available}$	*available pressure difference in pure hydrostatic pressure schedule*
$\Delta P_{required}$	*required pressure difference for purely hydrostatic operation*
R_{film}	*resistance of the journal-bearing gap (electric analogy)*
$R_{restrictor}$	*resistance of the restrictor (electric analogy)*
α	*fraction of the turbine gage pressure supplied to the high pressure plenum*
β	*fraction of the turbine gage pressure supplied to the low pressure plenum*

$D = d/dt$	*differential operator with respect to time*
$F_{hydrostatic}$	*hydrostatic restoring force*
$F_{hydrostatic\_L\&R}$	*hydrostatic restoring force based on the Larson and Richardson model*
τ_1	*lead time constant*
τ_2	*lag time constant*

d	*separation between journal and aft plate*
u	*velocity of the flow between journal and aft plate*
u_o	*relative velocity between journal and aft plate*
y	*vertical location between journal and aft plate*
A_{wet}	*surface area over which Couette flow between the journal and aft plate is assumed to exist*
F_{shear}	*shear force acting on journal due to aft plate*
τ	*shear stress*

$$W_r = \frac{w_r}{\mu \varpi r L}\psi^2 = \left(\frac{12\zeta}{\Lambda}\right) \qquad \textit{Sommerfeld Number}$$

$$\Lambda = \frac{6\mu\omega}{\psi^2 P_a} \qquad \textit{Bearing Number}$$

$$\zeta = \frac{w_r}{2rLP_a} \qquad \textit{Load Parameter}$$

$$\overline{M} = \frac{mP_a}{72L\mu^2}\psi^5 \qquad \textit{Mass Parameter}$$

$\overline{\Omega} = \overline{\Omega}_d + i\overline{\Omega}_v$ *eigenvalues of governing matrix*

$\overline{\Omega}_d$ *stability parameter (* $\overline{\Omega}_d > 0 \Rightarrow$ *Unstable;* $\overline{\Omega}_d < 0 \Rightarrow$ *Stable)*

$\overline{\Omega}_v = \dfrac{\omega_{whirl}}{\omega}$ *whirl ratio*

$\dfrac{1}{\overline{\Omega}_v} = \dfrac{\omega}{\omega_{whirl}}$ *critical speed ratio*

Stiffness and Damping Coefficients:

$k_{xx} = \dfrac{\partial w_x}{\partial x}$ $\quad k_{zz} = \dfrac{\partial w_z}{\partial z}$ $\quad k_{xz} = \dfrac{\partial w_x}{\partial z}$ $\quad k_{zx} = \dfrac{\partial w_z}{\partial x}$

$b_{xx} = \dfrac{\partial w_x}{\partial \dot{x}}$ $\quad b_{zz} = \dfrac{\partial w_z}{\partial \dot{z}}$ $\quad b_{xz} = \dfrac{\partial w_x}{\partial \dot{z}}$ $\quad b_{zx} = \dfrac{\partial w_z}{\partial \dot{x}}$

Other forms of Stiffness and Damping Coefficients:

$K_{ij} = \dfrac{c}{w_r} k_{ij}$ *conventional form of dimensionless stiffness coefficients*

$\overline{K}_{ij} = \dfrac{\zeta}{\Lambda} K_{ij}$ *dimensionless stiffness coefficients*

$B_{ij} = \dfrac{c\omega}{w_r} b_{ij}$ *conventional form of dimensionless damping coefficients*

$\overline{B}_{ij} = \dfrac{\zeta}{\Lambda} B_{ij}$ *dimensionless damping coefficients*

$\overline{B}_{ext}$ *external damping*

CHAPTER 1

INTRODUCTION

1.1 M.I.T. Microengine Project

MIT is active in the development of micro-electro-mechanical systems (MEMS)–based gas turbine engines and turbo-generators. These devices will be manufactured using semiconductor micro-fabrication procedures and will be produced in large numbers. Mechanically, they are based on high speed rotating turbo-machinery. Figures (1-1 and 1-2) depict the gas turbine engine and the flow path through it.[1,2]

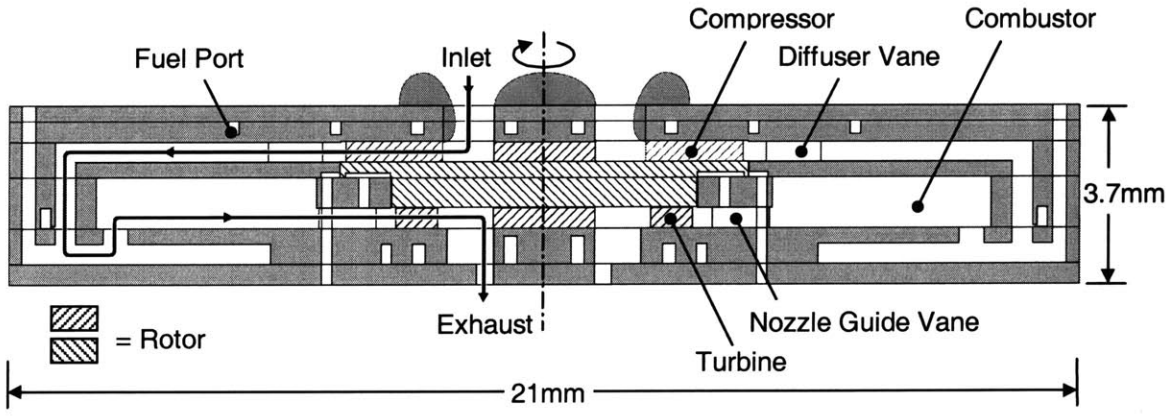

Figure 1-1: Cross-section diagram of the microengine turbojet.[3,4]

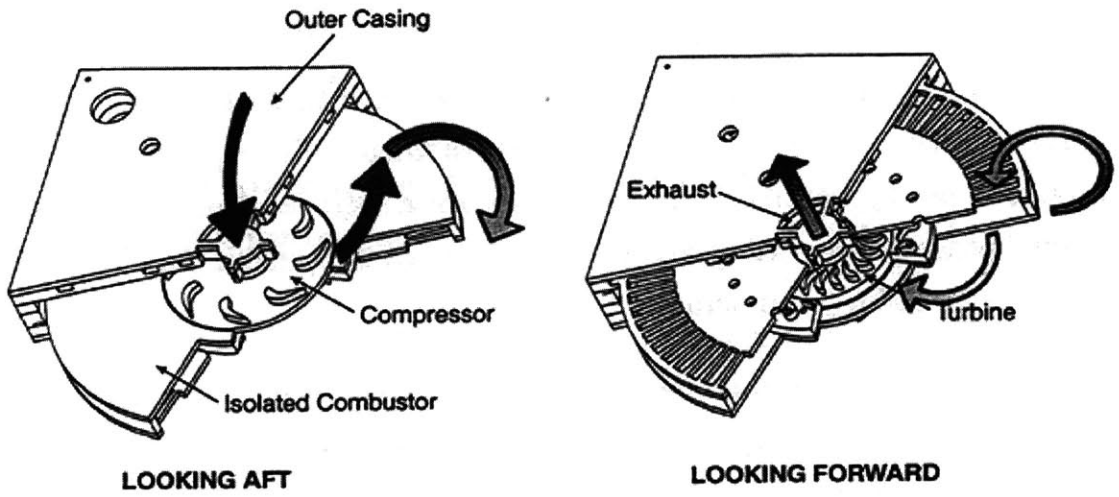

Figure 1-2: 3-D diagram of the demonstration turbojet, depicting a radial outflow compressor and a radial inflow turbine.[3]

Air enters through the inlet and then passes through the compressor, which increases its stagnation pressure. The flow is then diffused through the diffuser vanes and travels radially outwards until it reaches the edge of the engine, where its direction is reversed so as to make it enter the combustor, where it is burned with hydrogen. The air then travels through the turbine nozzle guide vanes, and is expanded in the turbine blades, which use the flow's energy to drive the compressor. Finally, the flow is exhausted through the exhaust ports. For the gas turbine engine, the exhausted flow has remaining energy in it, which is used to produce thrust. In the turbo-generator, where a micro-generator – used to produce electricity – is inserted inside the engine, the exhaust flow has little remaining energy in it, and as a result, marginal thrust is produced.

The microengine is fabricated by deep etching and bonding single-crystal silicon wafers.[5] It measures 21mm in diameter and 3.7mm in thickness. It has been designed to produce 11 grams of thrust (17W of power) with a pressure ratio of 2:1 and is expected to consume 16 grams/hour of H_2 (Table 1-1).[3] Once an operational engine is built, it is hoped that further refinement will allow the engine to produce over 50 Watts of electrical or propulsive power. Such power densities are similar to those of large aircraft engines and ground-based turbine generators.

Table 1-1: Demonstration turbojet characteristics.[4]

Parameter	Micro-Engine Value
Thrust	11g
Fuel burn (Hydrogen)	16g/hr
Engine weight	2g
Turbine inlet temperature (T_{T4})	1600 K (2421°F)
Exhaust gas temperature	970°C
Rotor angular speed	1,200,000 rpm

The microengine turbojet has many applications including the propulsion of micro air vehicles such as the one shown in Figure (1-3). The propulsive efficiency of the turbojet at the low flight speeds required by such vehicles is estimated to be less than 20%.[4] However, the overall efficiency of the system will still be higher than that of any current micropropulsion system (such as electric motors powered by batteries).

Figure 1-3: Micro Air Vehicle (MAV) mock-up.[4] (courtesy of Prof. Drela)

Like the turbojet, the turbo-generator has many potential applications. For example, it could be used to produce portable electric power, replacing conventional batteries in a wide variety of consumer electronic devices as well as military equipment.[2] Preliminary calculations show that the turbo-generator could have approximately twenty times the energy density of a conventional battery.[4]

1.2 Motivation

Efficient operation of the microengine requires that the rotor tip Mach number be of order unity. For the 6mm diameter rotor used by the microengine, this translates to 1.2 million rpm.[4] Using conventional ball bearings is not an option because of excessively large frictional losses and high wear rates. However, two other solutions are available. The first, magnetic bearings, was deemed unfeasible due to its high level of complexity. Gas bearings were considered as the second option. In this solution, the rotor spins on a thin film of air that separates it from the stationary part of the engine. Although far from simple, gas bearings were chosen for the microengine.

The advantages of using gas bearings are that they have very low drag and little wear. However, they also have several disadvantages. First, making the rotor spin stably is challenging and can only be achieved under very specific conditions. Second, external pressure sources may be required to create the necessary conditions. Finally, and most importantly, the rotor must maintain stability while accelerating from rest to full speed.

Extensive research on this topic has been performed by Orr[6] and Piekos[15] at both the experimental and analytical level. The experiments confirmed the feasibility of gas bearings and the analytical research resulted in the production of several extensive numerical models predicting the gas bearing's behavior. To supplement the above models, however, a lower order model was also developed. It is able to simulate the operation of the bearing as a function of the speed, and quickly predict its performance trends, suggesting possible paths leading to full speed operation. It is this model that shall be discussed in this thesis.

1.3 Gas Bearings

1.3.1 Nomenclature and General Model

In order to proceed, it is important to define a few terms and describe the geometry of a gas bearing (Figure 1-4).

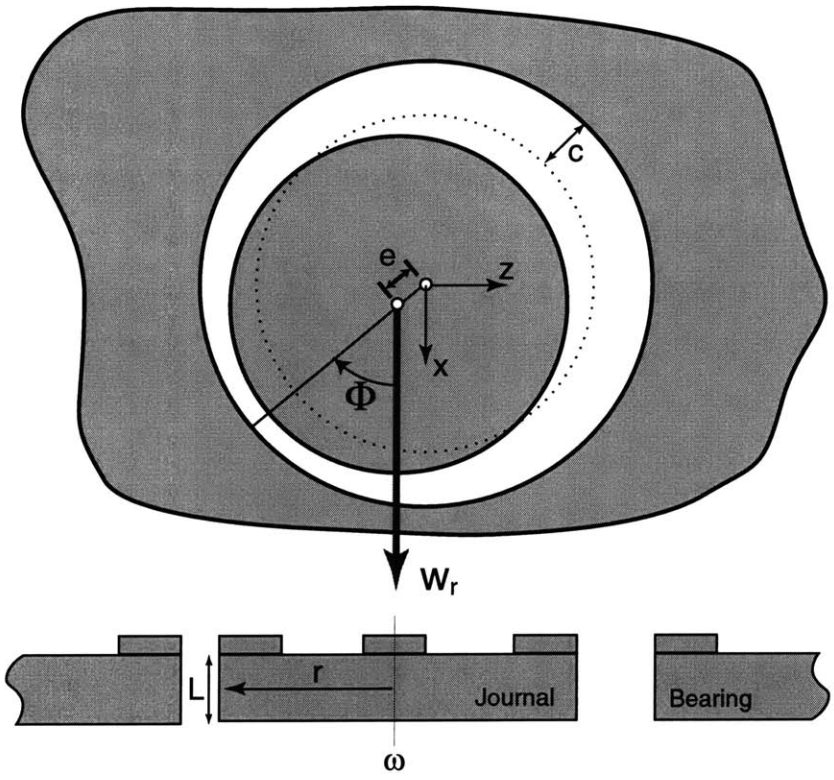

Figure 1-4: Gas bearing geometry and nomenclature

The journal (rotor) is the rotating part of the setup. It spins at an angular velocity, ω, inside of the bearing (stator) which is stationary. The journal's radius is r. Its length (or thickness) is L and its mass is m. When the journal's center is placed on the bearing's center, the spacing between the outer edges of the two, is called the clearance, c. The ambient pressure of the air surrounding the journal is denoted by P_a and the viscosity of the air by μ.

An external force, denoted by w_r, may be applied to the journal. A coordinate system is drawn such that the x-axis is parallel to the direction of this force. The external load may cause the journal's center to move away from the bearing's center. The distance between the two is called the eccentricity and is denoted by e. When the eccentricity is normalized by the clearance, the result is called the eccentricity ratio and is denoted by ε (where $\varepsilon = e/c$). The angle between the x-axis and the line connecting the journal center to the bearing center is called the attitude angle and is denoted by Φ. The ratio of the diameter to the length of the journal is called λ (where $\lambda = 2r/L$) and the ratio of the clearance to the radius is called ψ (where $\psi = c/r$).

1.3.2 Bearing Design

In order to achieve stable operation, it might be necessary to load the journal so as to make it operate in a hydrodynamic mode, where it spins at a non-zero eccentricity ratio. In conventional gas bearings this load can come from the weight of the journal itself. However, since our bearing is so small, its weight is insufficient. As a result, the journal is loaded by applying differential pressures to its surfaces. This is achieved by placing it on top of an aft plate (Figure 1-5) which, for the purposes of this analysis, consists of two separate plena which are externally pressurized. When different pressures are applied to these plena, the journal experiences a net load force and is pushed away from the center of the bearing. The pressure in the high pressure plenum is denoted by P_{PH} and the pressure in the low pressure plenum is denoted by P_{PL}.

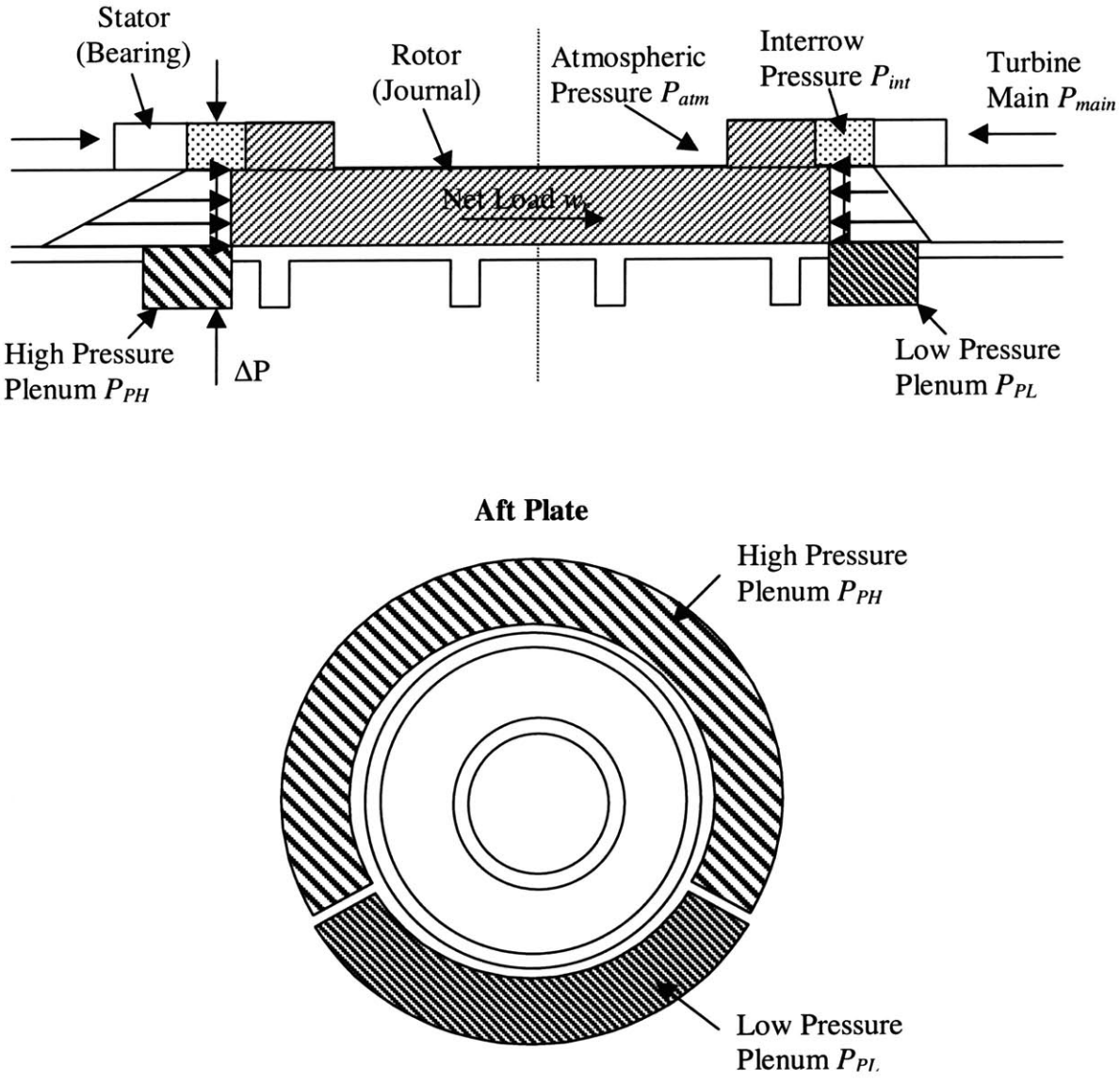

Figure 1-5: Bearing rig schematic: The aft plate consists of two separate plena which can be pressurized to any desired pressure, P_{PH} and P_{PL}. By applying different pressures to the plena the journal is loaded.

An external pressure source is also used to provide the main turbine air pressure, P_{main}, which drives the turbine. The pressure of the air between the stator and the turbine blades is called the interrow pressure, P_{int}. The pressure difference between the interrow pressure and the plena pressures is called the axial pressure difference and is denoted by ΔP. This pressure difference can drive an axial flow and is a source of hydrostatic stiffness. Finally, since the exhaust of the turbine is exposed to the surrounding

atmosphere, the turbine exhaust pressure is assumed to be atmospheric and is denoted by P_{atm}.

1.3.3 Bearing Rigs

In trying to make the engine operational, a macro-bearing rig was built by Orr[6], and a micro-bearing rig was built by Lin[7]. The purpose of the rigs was to validate bearing design tools and to study bearing and rotordynamic behavior in these systems. The rigs were constructed based on the schematic shown in Figure (1-5). The macro-rig is 26 times larger than the turbojet's turbine and uses conventional instrumentation. Experiments performed using this rig validated the feasibility of gas bearings for both hydrodynamic and hydrostatic operation. The micro-rig (Figure 1-6), on the other hand, is approximately the same size as the turbojet's turbine. Due to its size, instrumentation is very limited, something which makes its operation very cumbersome. Experiments using this rig are still underway and the latest runs reported a rotational speed of 1.4 million rpm. In this thesis, we will only be examining this rig. The following table summarizes most of its characteristics.

Table 1-2: Micro-bearing rig geometric parameters

Variable	**Micro-Bearing Rig Value**
Mass (m)	10 mg
Radius (r)	2.05 mm
Clearance (c)	12 μm
Length (L)	300 μm
Ratio (ψ)	5.85×10^{-3}
Ratio (λ)	13.3
Design Speed (ω_{design})	2,000,000 rpm

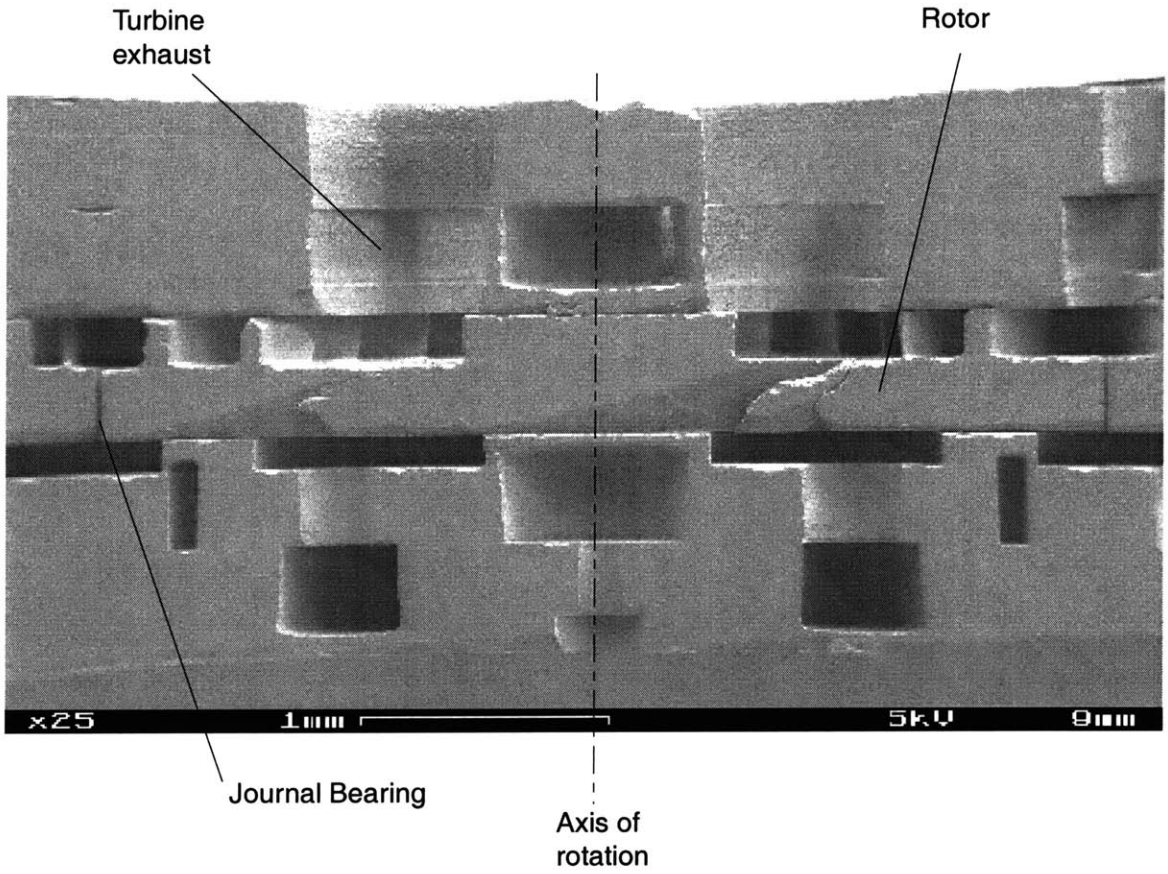

Figure 1-6: Micro-bearing rig die-cut cross-section. (courtesy of C.C. Lin)[7]

1.4 Modes of Operation

There are three modes of operation for gas bearings: hydrodynamic, hydrostatic, and hybrid. By varying the plena pressures in the bearing rig, we can control the mode of operation. Each mode has its own stability characterisitics.

1.4.1 Hydrodynamic Operation

Hydrodynamic operation is based on the inherent properties of the thin film of fluid separating the journal from the bearing.[8,9,10] Under this mode, the journal must operate off of the bearing's center and therefore must be loaded. Off center operation

results in an assymetric pressure distribution in the lubricating film. This opposes the externally applied load and thus introduces stiffness to the system. The eccentricity ratio adjusts itself until the two forces are equal. As would intuitively be expected, increasing the externally applied load results in an increase in the equilibrium eccentricity ratio.

In addition to providing stiffness to the journal, the pressure distribution also acts as a source of damping. Both of these effects increase with increasing eccentricity ratio and tend to infinity. This is fortunate because it means that any amount of stiffness or damping can be achieved by simply increasing the load. However, it is also unfortunate in the respect that the journal may have to operate extremely close to the bearing in order for appropriate levels of stiffness and damping to be developed.

The advantage of hydrodynamic operation is that the stiffness and damping arise from the rotor motion itself. However, there are two disadvantages. The first, and most important one, is that stable operation requires that the journal is spinning at high eccentricity ratios. The second one is that in order to achieve any eccentricity ratio the journal has to be externally loaded, something which may require the use of an external pressure source.

1.4.2 Hydrostatic Operation

Hydrostatic operation provides stiffness to the journal by supplying pressurized air to the journal-bearing gap.[11,12] The classical setup of a hydrostatic bearing is shown in Figure (1-7).

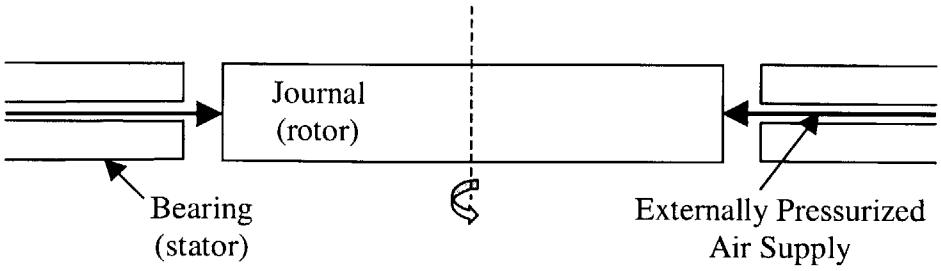

Figure 1-7: Center-injection hydrostatics. Externally pressurized air is supplied to the center of the journal, thus introducing hydrostatic stiffness.

Either an array of holes or a slot is made at the center of the bearing so as to allow the pressurized air to flow into the journal-bearing gap. This type of setup is called center injection hydrostatics.

In order to understand the principle of hydrostatic operation, the above system is modeled as a group of resistors (Figure 1-8), in which pressure acts as voltage and flow rate acts as current.

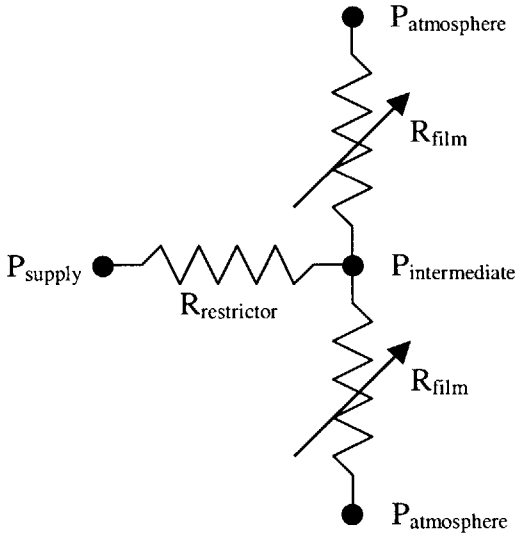

Figure 1-8: Hydrostatic operation / resistor analogy

The pressure of the air that is being provided to the journal-bearing gap is denoted by P_{supply} and is fixed by the operator. The holes providing the air to the gap act as restrictors and are modeled as a fixed resistance, $R_{restrictor}$. The pressure at which the air first contacts the journal is denoted by $P_{intermediate}$. As the air flows through the journal-bearing gap, there is another pressure drop that is a function of the film thickness. The film is therefore modeled as a variable resistance, R_{film}, which is directly related to the eccentricity ratio. Finally, the pressure of the air exiting the gap is fixed at atmospheric pressure, $P_{atmosphere}$. Since the pressure difference between $P_{atmosphere}$ and P_{supply} is fixed, the value of $P_{intermediate}$ is proportional to the ratio of the two resistances and increases as the eccentricity ratio increases. This effect introduces hydrostatic stiffness to the journal.

As the supply pressure increases, the hydrostatic stiffness of the system is also expected to increase. This is because a given change in eccentricity ratio results in a larger change in the intermediate pressure, and consequently a larger restoring force. Also, it is important to note that, unlike hydrodynamic operation, the stiffness is only moderately sensitive to the eccentricity ratio.

Another way hydrostatics can be introduced to the system is by supplying pressurized air at the end of the bearing instead of the center. This type of arrangement is called end-injection hydrostatics (Figure 1-9) and was first discovered in the macro-rig by Orr[6] and Piekos[15]. It is identical to center injection hydrostatics with the exception that there is only one film resistor instead of two. The current micro-bearing rig uses this form of hydrostatics.

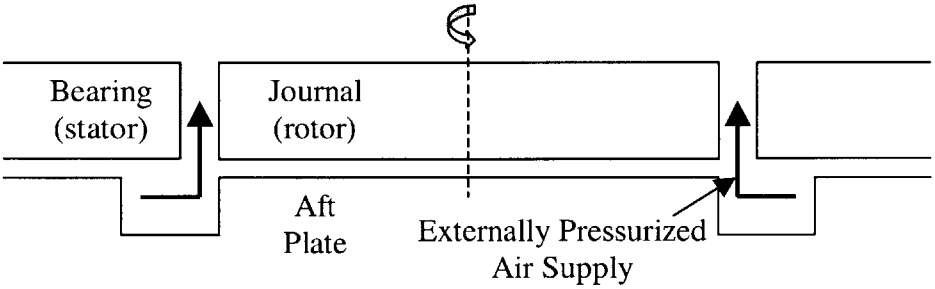

Figure 1-9: End-injection hydrostatics. Externally pressurized air is supplied to the end of the journal, thus introducing hydrostatic stiffness.

The advantages of hydrostatic operation are that the bearing operates at an eccentricity ratio of zero and that its stiffness can be directly controlled by simply adjusting the pressure in the plena. The disadvantage, however, is that an external pressure source is required.

1.4.3 Hybrid Operation

Hybrid operation refers to the situation where both hydrostatics and hydrodynamics are present. In fact, the bearing rig can only operate in a hybrid mode. Purely hydrodynamic operation cannot exist because the loading of the journal requires pressurized air in the plena, something which unavoidably introduces hydrostatic effects

to the system. Technically, purely hydrostatic operation also cannot exist because hydrodynamic effects, which are due to the inherent properties of the fluid film, are always present. However, at eccentricity ratios close to zero, these effects can be considered negligible.

1.5 Tools for Analysis

1.5.1 Analytical Solutions

Two common analytical solutions for hydrodynamic operation are offered by the Half and Full-Sommerfeld models.[8,9,10] Both models are based on the incompressible form of the Reynolds Equation and the Equation of Motion. The incompressible Reynolds Equation is based on the following assumptions:

- Viscous forces >> Inertial forces
- The fluid film is treated as having a constant viscosity
- Zero slip at the fluid-solid interface
- The curvature of the film is small (i.e. $r >> c$)
- Incompressible fluid

Both models are for incompressible fluids (i.e. liquid bearings), and they are identical, with the exception that the Half-Sommerfeld model assumes that the fluid cavitates along half of the journal-bearing interface – something which is commonly observed in liquid bearings. It is important to note that the assumption of an incompressible fluid makes these models invalid for our bearing. However, they provide a means of validating our model as well as some insight, as will be explained later on.

1.5.2 Low-Order Projection Solutions

The low order projection solutions are based on the compressible form of the Reynolds Equation coupled with the Equation of Motion.[6, 14] In solving these equations, the pressure film is represented as a truncated Fourier series where a Galerkin projection[13] is used to determine the coefficients. This results in a series of ordinary

differential equations based on which a linear stability analysis is performed. This type of analysis was initially performed by Cheng and Pan[13] and was extended by Jacobson[14] in order to get more precision. Later, Orr[6] extended the analysis even further and was able to get results that were identical to those of the full numerical simulation, that will be explained in the next section.

1.5.3 Full Numerical Simulation

The full numerical simulation, developed by Piekos,[15] is based on a compressible form of the Reynolds equation coupled with the Equation of Motion. It uses an orbit method, which is a numerical experiment in time. Its results are very precise, even at high eccentricity ratios. The only disadvantage of this code, is that it is very time costly.

1.6 Need for a Low Order Model

The tools that are available are mostly designed to analyze hydrodynamic and hydrostatic operation. However, our gas bearing can never operate in a pure hydrodynamic or hydrostatic mode. As a result, it was realized that there was a need for a low-order model capable of analyzing hybrid operation. This need resulted in the model we present. It draws upon the stiffness and damping coefficients predicted by the full numerical simulation and is capable of predicting the stability of the rotor under any operating condition. Due to its simplicity it is very fast but not very precise – especially at higher eccentricity ratios. Nonetheless, its purpose is to indicate trends in hybrid operation, and its most important aspect is that it is able to simulate the operation of the bearing as a function of the speed, once given a certain plena pressure schedule.

1.7 Thesis Outline

In Chapter 2 we introduce the mathematical basis of the model and the stiffness and damping coefficients upon which it relies. Further, we explain the procedure for going

from the plena pressures and the turbine main air pressure to determining wheather stable operation is achievable.

In Chapter 3 hydrodynamic and hydrostatic stability boundaries are constructed. Several hybrid pressure schedules are examined to determine the most feasible way for reaching full speed operation. Finally, in Chapter 4 we discuss our conclusions.

CHAPTER 2

STABILITY MODEL

In this chapter, we introduce the governing equations of our stability model. We then re-write them in non-dimensional form and explain how to solve them. Then, we examine the stiffness and damping coefficients that are available for our model and establish which ones will actually be used. Finally, we explain how to evaluate the stability characteristics of the bearing given the bearing's angular speed and plena pressures.

2.1 Governing Equations

We first assume that the journal is spinning in equilibrium with an external load, w_r, applied to it (Figure 1-4).[16] This load may be zero for the case of purely hydrostatic operation. The journal will also be experiencing an internal force due to hydrodynamics and/or hydrostatics. This reaction force is broken into its components in the x and z directions and is denoted as w_x and w_z respectively. Newton's second law of motion suggests the following:

$$\begin{pmatrix} m & 0 \\ 0 & m \end{pmatrix} \frac{\partial^2}{\partial t^2} \begin{pmatrix} e\cos\Phi \\ e\sin\Phi \end{pmatrix} = \begin{pmatrix} w_r \\ 0 \end{pmatrix} - \begin{pmatrix} w_x \\ w_z \end{pmatrix} \tag{2-1}$$

We then assume that the bearing is perturbed from its initial position by an amount Δx and Δz. To model this perturbation we perform a first-order Taylor expansion of w_x and w_z:

$$\begin{pmatrix} w_x \\ w_z \end{pmatrix} = \begin{pmatrix} (w_x)_o \\ 0 \end{pmatrix} + \begin{pmatrix} k_{xx} & k_{xz} \\ k_{zx} & k_{zz} \end{pmatrix} \begin{pmatrix} \Delta x \\ \Delta z \end{pmatrix} + \begin{pmatrix} b_{xx} & b_{xz} \\ b_{zx} & b_{zz} \end{pmatrix} \begin{pmatrix} \Delta \dot{x} \\ \Delta \dot{z} \end{pmatrix} \tag{2-2}$$

where:

$$k_{xx} = \frac{\partial w_x}{\partial x} \qquad k_{xz} = \frac{\partial w_x}{\partial z} \qquad b_{xx} = \frac{\partial w_x}{\partial \dot{x}} \qquad b_{xz} = \frac{\partial w_x}{\partial \dot{z}}$$

$$k_{zx} = \frac{\partial w_z}{\partial x} \qquad k_{zz} = \frac{\partial w_z}{\partial z} \qquad b_{zx} = \frac{\partial w_z}{\partial \dot{x}} \qquad b_{zz} = \frac{\partial w_z}{\partial \dot{z}} \tag{2-3}$$

Note that the first term in the expansion is based on the fact that the journal is initially in equilibrium (i.e. initially $w_r = (w_x)_o$ and $(w_z)_o = 0$).

Having expanded the right side of Eq. (2-1) into terms consisting of differentials in x and z the next step is to re-write the left side using similar terms. This is easily done when the following geometric relationship is considered:

$$\frac{\partial^2}{\partial t^2} \begin{pmatrix} e\cos\Phi \\ e\sin\Phi \end{pmatrix} = \begin{pmatrix} \Delta \ddot{x} \\ \Delta \ddot{z} \end{pmatrix} \tag{2-4}$$

Finally, substituting Eq. (2-2) and Eq. (2-4) into Eq. (2-1) and remembering that w_r is left unchanged by the perturbation (i.e. $w_r = (w_x)_o = \text{const.}$) the following equation results:

$$\begin{pmatrix} m & 0 \\ 0 & m \end{pmatrix} \begin{pmatrix} \Delta \ddot{x} \\ \Delta \ddot{z} \end{pmatrix} + \begin{pmatrix} b_{xx} & b_{xz} \\ b_{zx} & b_{zz} \end{pmatrix} \begin{pmatrix} \Delta \dot{x} \\ \Delta \dot{z} \end{pmatrix} + \begin{pmatrix} k_{xx} & k_{xz} \\ k_{zx} & k_{zz} \end{pmatrix} \begin{pmatrix} \Delta x \\ \Delta z \end{pmatrix} = \begin{pmatrix} 0 \\ 0 \end{pmatrix} \tag{2-5}$$

This is the governing equation of the system.

2.2 Non-Dimensional Form of the Governing Equation

In order to make the analysis more general, Eq. (2-5) is non-dimensionalized by introducing the following variables[16]:

$$x_{new} = \frac{x}{c} \qquad z_{new} = \frac{z}{c} \qquad \tau = t\omega \tag{2-6}$$

Furthermore, the following parameters (commonly used in the literature of bearing theory) are also introduced:

$$\textit{Bearing Number:} \qquad \Lambda = \frac{6\mu\omega}{\psi^2 P_a} \tag{2-7}$$

$$\textit{Mass Parameter:} \qquad \overline{M} = \frac{mP_a}{72l\mu^2}\psi^5 \tag{2-8}$$

$$\textit{Load Parameter:} \qquad \zeta = \frac{w_r}{2rlP_a} \tag{2-9}$$

$$\textit{Sommerfeld Number:} \qquad W_r = \frac{w_r}{\mu\omega rl}\psi^2 = 12\frac{\zeta}{\Lambda} \tag{2-10}$$

For a fixed geometry, the bearing number may be thought of as the dimensionless form of the speed. The mass parameter, as the dimensionless form of the mass of the journal, and the load parameter as the dimensionless form of the externally applied load. Finally, the Sommerfeld number is a function of several variables and turns out to be twelve times the ratio of the load parameter to the bearing number. It is a particularly useful variable because the incompressible theory (Half-Sommerfeld or Full-Sommerfeld) predicts a unique relationship between W_r and the eccentricity ratio. As a result, any combination of two of the variables ζ, Λ and ε, can be used to solve for the third through an application of Eq. (2-10) and one of the incompressible models.

The next step is to introduce nondimensional forms of the stiffness and damping coefficients:

$$K_{ij} = \frac{c}{w_r} k_{ij} \qquad B_{ij} = \frac{c\omega}{w_r} b_{ij} \tag{2-11}$$

$$\overline{K}_{ij} = \frac{\zeta}{\Lambda}\left[\frac{c}{w_r} k_{ij}\right] \qquad \overline{B}_{ij} = \frac{\zeta}{\Lambda}\left[\frac{c\omega}{w_r} b_{ij}\right] \tag{2-12}$$

The first set of expressions are the conventional form of the non-dimensional stiffness and damping coefficients. However, they are not used because they tend to infinity at an eccentricity ratio of zero. This would complicate the analysis significantly, especially when examining hydrostatic operation. This effect is due to the fact that the externally applied load appears in the denominator of the expressions and its value is zero at an eccentricity ratio of zero. In order to remedy this problem, we will be using the conventional stiffness and damping coefficients multiplied by the ratio of the load parameter to the bearing number.

Finally, the dimensionless form of the governing equation is obtained using Eq.'s (2-5, 2-6, 2-7, 2-8, 2-9, and 2-12):

$$\begin{pmatrix} \Lambda\overline{M} & 0 \\ 0 & \Lambda\overline{M} \end{pmatrix}\begin{pmatrix} \Delta\ddot{x} \\ \Delta\ddot{z} \end{pmatrix} + \begin{pmatrix} \overline{B}_{xx} & \overline{B}_{xz} \\ \overline{B}_{zx} & \overline{B}_{zz} \end{pmatrix}\begin{pmatrix} \Delta\dot{x} \\ \Delta\dot{z} \end{pmatrix} + \begin{pmatrix} \overline{K}_{xx} & \overline{K}_{xa} \\ \overline{K}_{zx} & \overline{K}_{zz} \end{pmatrix}\begin{pmatrix} \Delta x \\ \Delta z \end{pmatrix} = \begin{pmatrix} 0 \\ 0 \end{pmatrix} \tag{2-13}$$

x and z refer to x_{new} and z_{new} respectively and continue to do so throughout the rest of this thesis.

The above equation depends on the bearing number which is treated as an independent variable, the mass parameter which is mainly a function of the geometry, and the stiffness and damping coefficients which are only functions of the eccentricity ratio and the bearing number (this will be shown later).

2.3 Solution Forms and Their Interpretation

In order to solve Eq. (2-13), the following variables are introduced:

$$\begin{pmatrix} \Delta x_1 \\ \Delta z_1 \end{pmatrix} = \begin{pmatrix} \Delta \dot{x} \\ \Delta \dot{z} \end{pmatrix} \tag{2-14}$$

Using these two new variables, (Eq. 2-13) can be re-written in the form:

$$\underline{\dot{X}} = A\underline{X} \tag{2-15}$$

$$\begin{pmatrix} \Delta \dot{x} \\ \Delta \dot{x}_1 \\ \Delta \dot{z} \\ \Delta \dot{z}_1 \end{pmatrix} = \begin{pmatrix} 0 & 1 & 0 & 0 \\ -\frac{\overline{K}_{xx}}{\Lambda \overline{M}} & -\frac{\overline{B}_{xx}}{\Lambda \overline{M}} & -\frac{\overline{K}_{xz}}{\Lambda \overline{M}} & -\frac{\overline{B}_{xz}}{\Lambda \overline{M}} \\ 0 & 0 & 0 & 1 \\ -\frac{\overline{K}_{zx}}{\Lambda \overline{M}} & -\frac{\overline{B}_{zx}}{\Lambda \overline{M}} & -\frac{\overline{K}_{zz}}{\Lambda \overline{M}} & -\frac{\overline{B}_{zz}}{\Lambda \overline{M}} \end{pmatrix} \begin{pmatrix} \Delta x \\ \Delta x_1 \\ \Delta z \\ \Delta z_1 \end{pmatrix} \tag{2-16}$$

Now, the normal mode solution of Eq. (2-16) is of the following form:

$$\begin{pmatrix} \Delta x \\ \Delta x_1 \\ \Delta z \\ \Delta z_1 \end{pmatrix} = \begin{pmatrix} x_h \\ x_{h1} \\ z_h \\ z_{h1} \end{pmatrix} e^{\overline{\Omega} \omega t} \tag{2-17}$$

where $\overline{\Omega} = \dfrac{\Omega}{\omega}$; x_h, x_{h1}, z_h, z_{h1} are constants (2-18)

$\overline{\Omega}$ is the set of eigenvalues of the matrix A in Eq. (2-16). It consists of four numbers, some or all of which can be complex conjugate pairs and can be re-written as follows:

$$\overline{\Omega} = \overline{\Omega}_d + i\overline{\Omega}_w \tag{2-19}$$

The solution shown in Eq. (2-17) can also be written as:

$$\begin{pmatrix} \Delta x \\ \Delta x_1 \\ \Delta z \\ \Delta z_1 \end{pmatrix} = \begin{pmatrix} x_h \\ x_{h1} \\ z_h \\ z_{h1} \end{pmatrix} \left(e^{\overline{\Omega}_d \omega t}\right)\left(\cos(\overline{\Omega}_w \omega t) + i\sin(\overline{\Omega}_w \omega t)\right) \tag{2-20}$$

The real part of each of the eigenvalues, $\overline{\Omega}_d$, is the damping and corresponds to how quickly a perturbation of the journal decays or grows. Although there are four eigenvalues, only the one with the most positive real part is examined. This is because it only takes one unstable mode to make the journal go unstable. If the real part of that eigenvalue is less than zero, the system is classified as stable and if it is greater than zero, the system is classified as unstable.

The existence of an imaginary part in the eigenvalues implies that a perturbation will also cause the rotor center to start whirling around its initial position. The dimensional whirling frequency is $\overline{\Omega}_w \omega$. $\overline{\Omega}_w$ itself will be called the *whirl ratio* and its inverse will be called the *critical speed ratio*. Depending on the operating point being examined, the journal can be whirling at one or two differently damped frequencies. Unless otherwise noted, only the less-damped whirling frequency shall be considered since it is the one that is most likely to be observed in an experiment.

2.4 Stiffness/Damping Models

In the previous section, we showed how the value of $\overline{\Omega}$ determines the bearing's whirling frequency and whether it can operate stably. We also showed that this

parameter depends on the values of the stiffness and damping coefficients. Therefore, our model has to draw upon stiffness and damping coefficients predicted by other models or simulations.

2.4.1 Hydrodynamic Stiffness Coefficients

Hydrodynamic dimensionless stiffness coefficients based on the Half-Sommerfeld model, the Full-Sommerfeld model, and the full numerical simulation were examined.[15,16,17] The equations describing the stiffness coefficients for the Half and Full-Sommerfeld models are listed below:[16]

Half-Sommerfeld Model:

$$K_{xx} = \frac{4}{W_r\lambda^2}\left[\frac{\varepsilon \sin^2\Phi}{(1-\varepsilon^2)^2} + \frac{3\pi\varepsilon^2 \sin\Phi\cos\Phi}{4(1-\varepsilon^2)^{5/2}} + \frac{2\varepsilon(1+\varepsilon^2)\cos^2\Phi}{(1-\varepsilon^2)^3}\right] \tag{2-21}$$

$$K_{xz} = \frac{4}{W_r\lambda^2}\left[\frac{\pi(1+2\varepsilon^2)}{4(1-\varepsilon^2)^{5/2}}\sin^2\Phi + \frac{\varepsilon(1+3\varepsilon^2)}{(1-\varepsilon^2)^3}\sin\Phi\cos\Phi + \frac{\pi\cos^2\Phi}{4(1-\varepsilon^2)^{3/2}}\right] \tag{2-22}$$

$$K_{zx} = \frac{4}{W_r\lambda^2}\left[-\frac{\pi\sin^2\Phi}{4(1-\varepsilon^2)^{3/2}} + \frac{\varepsilon(1+3\varepsilon^2)}{(1-\varepsilon^2)^3}\sin\Phi\cos\Phi - \frac{\pi(1+2\varepsilon^2)\cos^2\Phi}{4(1-\varepsilon^2)^{5/2}}\right] \tag{2-23}$$

$$K_{zz} = \frac{4}{W_r\lambda^2}\left[\frac{2\varepsilon(1+\varepsilon^2)}{(1-\varepsilon^2)^3}\sin^2\Phi - \frac{3\pi\varepsilon^2\sin\Phi\cos\Phi}{4(1-\varepsilon^2)^{5/2}} + \frac{\varepsilon\cos^2\Phi}{(1-\varepsilon^2)^2}\right] \tag{2-24}$$

where, $W_r = \frac{1}{\lambda^2}\frac{\varepsilon\left[16\varepsilon^2+\pi^2(1-\varepsilon^2)\right]^{1/2}}{(1-\varepsilon^2)^2}$ and $\Phi = \tan^{-1}\left[\frac{\pi(1-\varepsilon^2)^{1/2}}{4\varepsilon}\right]$ (2-25,26)

Full-Sommerfeld Model:

$$K_{xx} = \frac{2}{W_r\lambda^2}\left[\frac{3\pi\varepsilon^2}{(1-\varepsilon^2)^{5/2}}\sin\Phi\cos\Phi\right] \tag{2-27}$$

$$K_{xz} = \frac{2}{W_r\lambda^2}\left[\frac{\pi(1+2\varepsilon^2)}{(1-\varepsilon^2)^{5/2}}\sin^2\Phi + \frac{\pi}{(1-\varepsilon^2)^{3/2}}\cos^2\Phi\right] \tag{2-28}$$

$$K_{zx} = \frac{2}{W_r \lambda^2}\left[\frac{\pi}{(1-\varepsilon^2)^{3/2}}\sin^2\Phi + \frac{\pi(1+2\varepsilon^2)}{(1-\varepsilon^2)^{5/2}}\cos^2\Phi\right] \tag{2-29}$$

$$K_{zz} = \frac{2}{W_r \lambda^2}\left[\frac{3\pi\varepsilon^2}{(1-\varepsilon^2)^{5/2}}\sin\Phi\cos\Phi\right] \tag{2-30}$$

where, $W_r = \dfrac{2\pi\varepsilon}{\lambda^2(1-\varepsilon^2)^{3/2}}$ and $\Phi = 90^o$ (2-31,32)

Figure (2-1) depicts the coefficients based on all three models. The plots for the full numerical simulation were extracted by Breuer[17] from Piekos'[15] analysis.

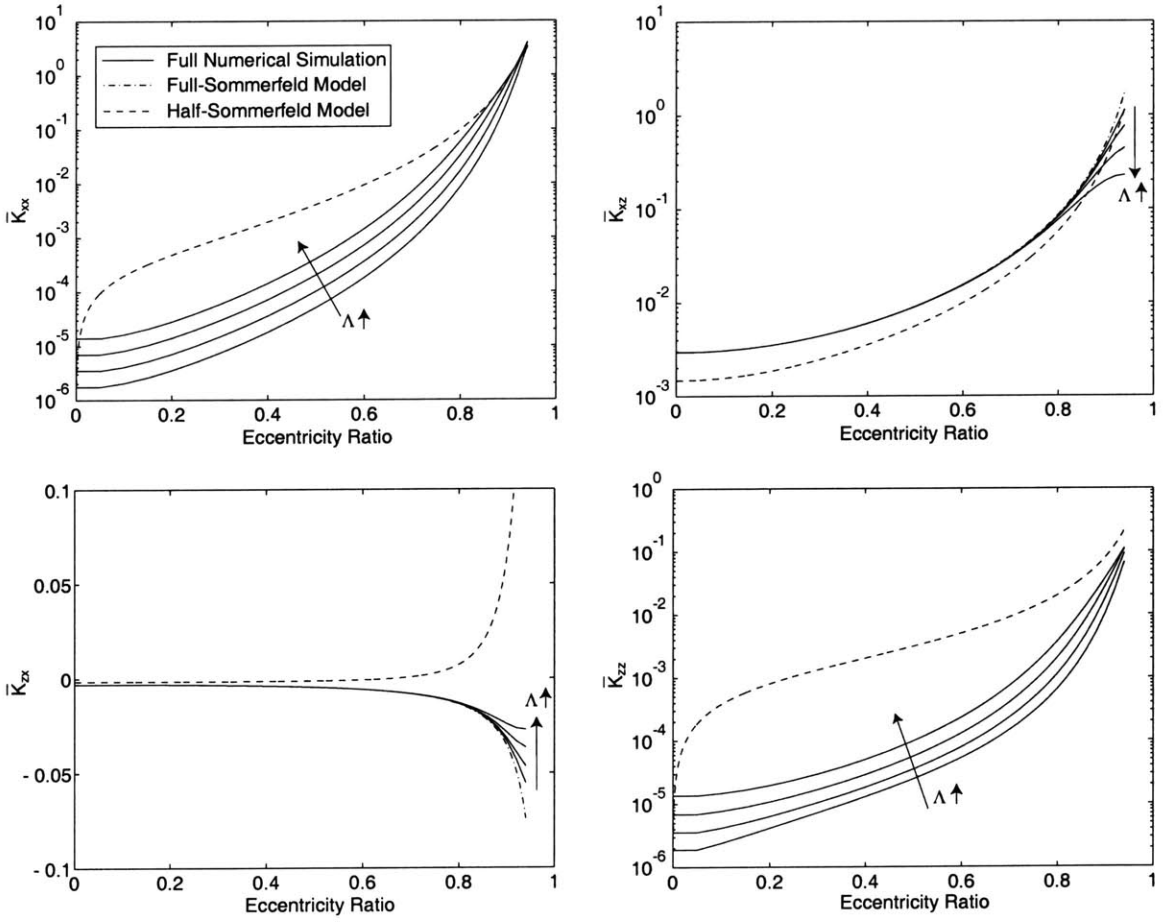

Figure 2-1: Hydrodynamic dimensionless stiffness coefficients based on the Half-Sommerfeld model, the Full-Sommerfeld model and the full numerical simulation, where λ=13.3. The results of the full numerical simulation are for bearing numbers of 0.25, 0.5, 1.0, and 2.0. Also note that for the Full-Sommerfeld model, K_{xx}=K_{zz}=0.

According to the Half and Full-Sommerfeld models, the stiffness coefficients are only functions of the eccentricity ratio. Further, they increase with increasing eccentricity ratio. The models differ only because the Half-Sommerfeld model assumes that the bearing cavitates. According to the Full-Sommerfeld model, the bearing has only cross-stiffness. This means that whenever the journal is pushed in any direction, the internal hydrodynamic forces will respond by creating a restoring force acting perpendicular to the perturbation. This behavior does not allow for stable operation (at any speed). However, in the Half-Sommerfeld model the assumed cavitation has the effect of introducing direct stiffness to the bearing and as a result stable operation is achievable.

Like the Half and Full-Sommerfeld models, the full numerical simulation shows that the stiffness coefficients increase with increasing eccentricity ratio. However, it further demonstrates that they are also functions of the bearing number. This dependence on the bearing number arises due to compressibility effects which were not accounted for in the Half and Full-Sommerfeld models. More specifically, it shows that the bearing has direct stiffness which increases with increasing bearing number. It also predicts cross stiffness coefficients which are identical to the ones predicted by the Full-Sommerfeld model at eccentricity ratios below 0.8. At higher eccentrcity ratios, compressibility effects take an increasingly important role and the two models predict different results. For our low-order model, the stiffness coefficients from the full numerical simulation are used since they most accurately represent the bearing. However the Half and Full-Sommerfeld models will also be used for validation purposes.

An interesting result, based on the full numerical simulation, comes when the non-dimensional direct stiffness', in their conventional form (K_{xx} and K_{zz}), are divided by the bearing number. Figure (2-2) depicts the results for K_{xx}:

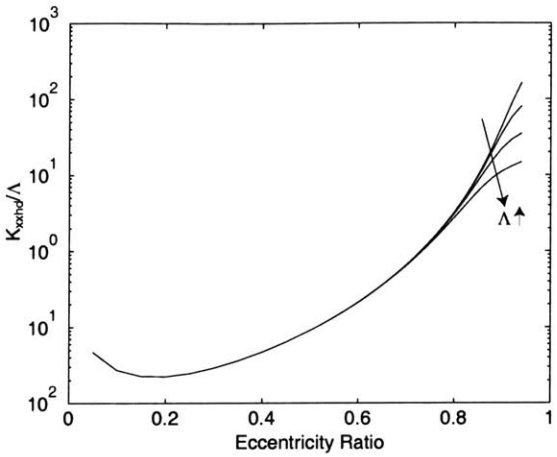

Figure 2-2: Hydrodynamic dimensionless direct stiffness (in conventional form) divided by the bearing number, based on the full numerical simulation for bearing numbers of 0.25, 0.5, 1.0, and 2.0, where λ=13.3. At low eccentricity ratios all the stiffness curves collapse onto a single curve.

At eccentricity ratios below 0.8, all the curves collapse onto a single line. This happens because the bearing has such a large ratio of diameter to length.[17] Since the full numerical simulation stiffness coefficients are only available for bearing numbers 0.25, 0.5, 1.0, and 2.0, it is necessary to sometimes extrapolate the direct stiffness coefficients for a certain bearing number by simply using the stiffness coefficient values from one of the known bearing numbers. More specifically, when examining the direct stiffness coefficients at bearing numbers between 0.25 and 2, interpolation procedures are used. However, when examining the direct stiffness coefficients at bearing numbers either below 0.25 or above 2.0 the following simple extrapolative equations are used:

For $\Lambda < 0.25$:

$$K_{ii} = \frac{\Lambda}{0.25} K_{ii}\Big|_{\Lambda = 0.25}$$

For $\Lambda > 2.0$:

$$K_{ii} = \frac{\Lambda}{2.0} K_{ii}\Big|_{\Lambda = 2.0} \qquad (2\text{-}33)$$

The cross stiffness coefficients are treated in the exact same way as the direct stiffness coefficients with the exception that the $\overline{K_{ij}}$ plots already collapse onto a single curve for eccentricity ratios below 0.8. As a result the extrapolative problem is solved much more easily.

It is important to realize, however, that when looking at stiffness coefficients that are either below a bearing number of 0.25, or above a bearing number of 2.0, and simultaneously at eccentricity ratios above 0.8, the results are subject to some error. This error, however, is negligble at the low bearing numbers and relatively small at the larger bearing numbers.

In Figure (2-3) the Sommerfeld number, as function of the eccentricity ratio (and bearing number), has been plotted for all three models. The Sommerfeld number increases monotonically with increasing eccentricity ratio according to all of the models. This implies that for a given bearing number, if the load is increased, the eccentricity ratio is also expected to increase

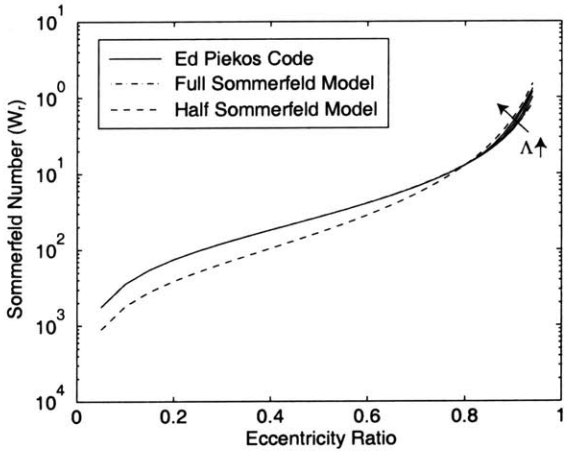

Figure 2-3: Sommerfeld number ($12\zeta/\Lambda$) based on the Half-Sommerfeld model, the Full-Sommerfeld model and the full numerical simulation. The results of the full numerical simulation are for bearing numbers of 0.25, 0.5, 1.0, and 2.0, where λ=13.3.

As expected, the Half-Sommerfeld results differ slightly from the Full-Sommerfeld results. However, what is interesting is that the full numerical simulation predicts idendtical Sommerfeld numbers as those of the Full-Sommerfeld model up to an eccentricity ratio of 0.8, at which point, once agaain, compressibility effects take an increasingly important role.

2.4.2 Hydrostatic Stiffness Coefficients

A code developed by Piekos[15], is used to determine the hydrostatic stiffness coefficients. This code predicts the relationship between the natural frequency of the journal as a function of the axial pressure difference, ΔP, and the value of λ. The relationship is relatively insensitive to the eccentricity ratio and is depicted for our gas bearing (λ = 13.3) in Figure (2-4). For the purposes of this thesis a fourth order polynomial was fit to it:

$$\omega_n = -0.0053\Delta p^4 + 0.320\Delta p^3 - 9.867\Delta p^2 + 282\Delta p \tag{2-34}$$

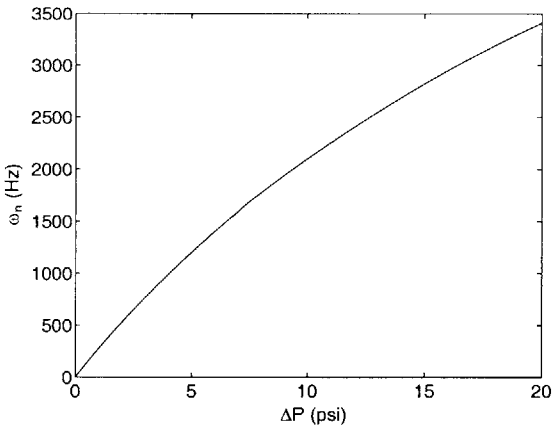

Figure 2-4: Hydrostatic natural frequency of the journal as a function of the axial pressure difference

As a result, once the pressure difference across the bearing is known, it is possible to determine the expected natural frequency of the journal, assuming that there are no hydrodynamic forces acting upon it. Once the natural frequency is determined, from Eq. (2-34), the next step is to determine the actual hydrostatic stiffness of the system. This is done by using the following simple equation:

$$k = \omega_n^2 m \tag{2-35}$$

Also, since the setup is symmetric, the stiffness coefficient in the x-direction has to be the same as the stiffness coefficient in the z-direction:

$$k_{xx} = k_{zz} = k \tag{2-36}$$

Finally, the above stiffness coefficients are converted to the non-dimensional form by using Eq. (2-37), which results from Eq's. (2-3, 2-6, and 2-12)):

$$\overline{K}_{ii} = \frac{\psi}{2LP_a\Lambda} k_{ii} \tag{2-37}$$

Figure (2-5) shows both the hydrodynamic and hydrostatic direct stiffness coefficients for bearing numbers of 0.25 and 2.0 and for axial pressure differences of 1psi and 5psi:

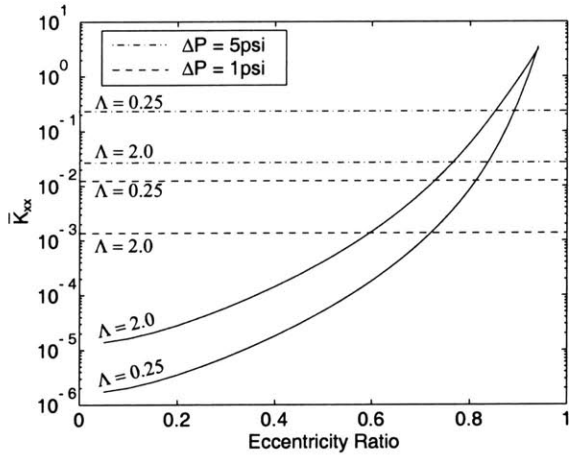

Figure 2-5: Hydrodynamic and hydrostatic stiffness coefficients for Λ = 0.25, 2.0 and ΔP= 1psi, 5psi. At low bearing numbers the hydrostatic dimensionless stiffness can be substantial, but as the bearing number increases, the hydrodynamic dimensionless stiffness becomes increasingly important.

As can be seen, at low bearing numbers the hydrostatic dimensionless stiffness can take on very large values, comparable (and in some cases larger) than the hydrodynamic dimensionless stiffness coefficient. However, as the bearing number increases the value of the hydrostatic dimensionless stiffness decreases, thus making hydrodynamics take an increasingly important role.

2.4.2.1 *Better Models for Hydrostatics*

In our model, we assume that the effect of the axial pressure difference, ΔP, is to introduce a restoring force which is equal to the stiffness, due to the pressure difference, multiplied by the journal's displacement:

$$F_{hydrostatic} = -kx \tag{2-38}$$

However, in a paper written by Larson and Richardson,[11,12] it is suggested that this force is not just a function of the hydrostatically induced stiffness and displacement. Instead, it is given by:

$$F_{hydrostatic\_L\ \&\ R} = -k\left(\frac{\tau_1 D+1}{\tau_2 D+1}\right)x \tag{2-39}$$

where $\tau_1$and τ_2 are lead and lag time constants which are based on the geometry of the bearing, and D is a differential operator with respect to time ($D = d/dt$). Their analysis is based on the fact that it takes a finite amount of time for the film pressures to change in response to the motion of the journal. This suggests that the bearing should portray signs of viscoelastic behavior, something which is not accounted for in our model.

2.4.3 Hydrodynamic Damping Coefficients

It was not possible to extract hydrodynamic damping coefficients from the full numerical simulation. As a result the only available damping coefficients were the ones from the Half and Full-Sommerfeld models. The equations describing these coefficients are listed below.[16]

Half Sommerfeld:

$$B_{xx} = \frac{4}{W\lambda^2}\left[\frac{\pi\sin^2\Phi}{2(1-\varepsilon^2)^{3/2}} + \frac{4\varepsilon\sin\Phi\cos\Phi}{(1-\varepsilon^2)^2} + \frac{\pi(1+2\varepsilon^2)\cos^2\Phi}{2(1-\varepsilon^2)^{5/2}}\right] \tag{2-40}$$

$$B_{xz} = B_{zx} = \frac{4}{W_r \lambda^2}\left[\frac{2\varepsilon \sin^2\Phi}{(1-\varepsilon^2)^2} - \frac{3\pi\varepsilon^2 \sin\Phi\cos\Phi}{2(1-\varepsilon^2)^{5/2}} - \frac{2\varepsilon\cos^2\Phi}{(1-\varepsilon^2)^2}\right] \tag{2-41}$$

$$B_{zz} = \frac{4}{W_r \lambda^2}\left[\frac{\pi(1+2\varepsilon^2)\sin^2\Phi}{2(1-\varepsilon^2)^{5/2}} - \frac{4\varepsilon \sin\Phi\cos\Phi}{(1-\varepsilon^2)^2} + \frac{\pi\cos^2\Phi}{2(1-\varepsilon^2)^{3/2}}\right] \tag{2-42}$$

Full Sommerfeld:

$$B_{xx} = \frac{4}{W_r \lambda^2}\left[\frac{\pi}{(1-\varepsilon^2)^{3/2}}\sin^2\Phi + \frac{\pi(1+2\varepsilon^2)}{(1-\varepsilon^2)^{5/2}}\cos^2\Phi\right] \tag{2-43}$$

$$B_{xz} = B_{zx} = \frac{4}{W_r \lambda^2}\left[\frac{3\pi\varepsilon^2}{(1-\varepsilon^2)^{5/2}}\sin\Phi\cos\Phi\right] \tag{2-44}$$

$$B_{zz} = \frac{4}{W_r \lambda^2}\left[\frac{\pi(1+2\varepsilon^2)}{(1-\varepsilon^2)^{5/2}}\sin^2\Phi + \frac{\pi\cos^2\Phi}{(1-\varepsilon^2)^{3/2}}\right] \tag{2-45}$$

Figure (2-6) depicts these coefficients.

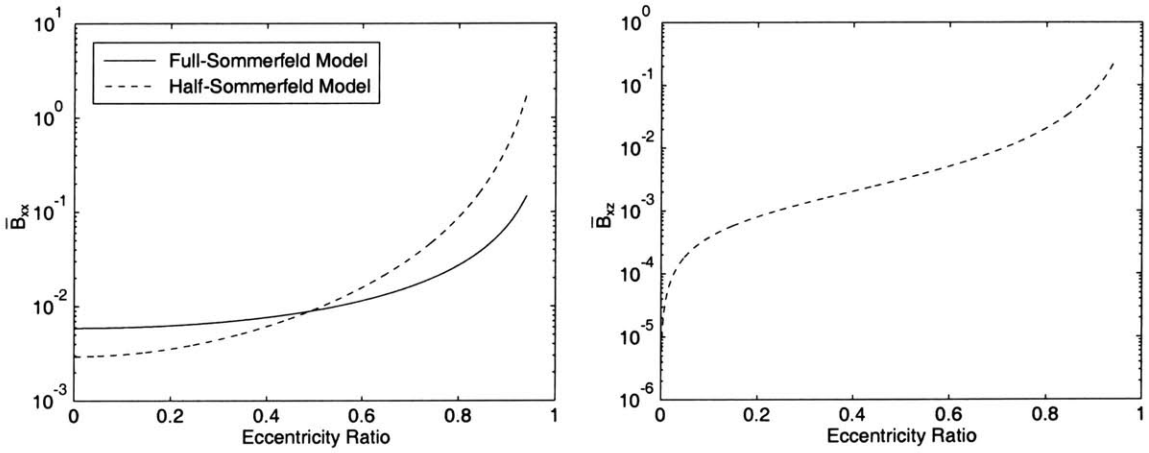

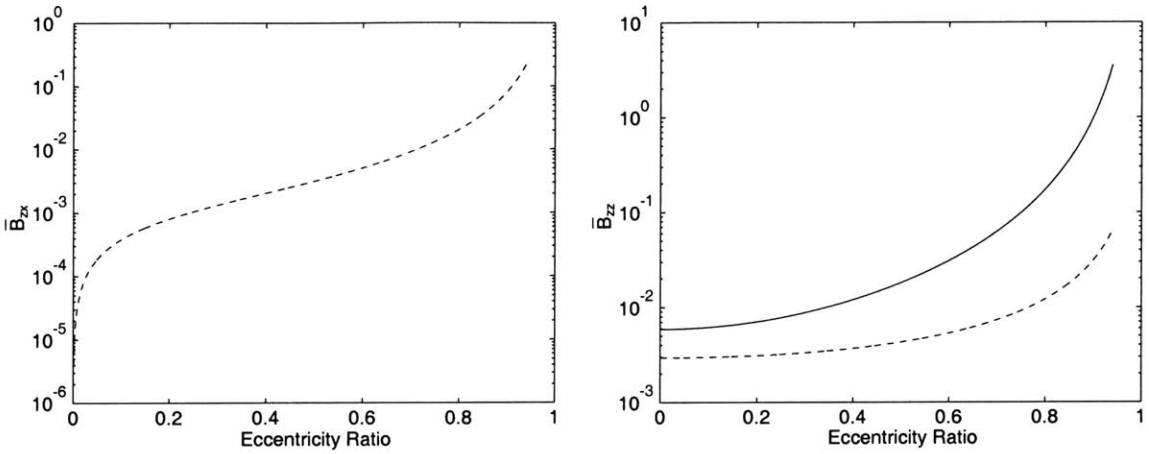

Figure 2-6: Hydrodynamic dimensionless damping coefficients based on the Half and Full-Sommerfeld models.

As expected, both the models predict that the damping coefficients are only functions of the eccentricity ratio, and increase with increasing eccentricity ratio. The Half-Sommerfeld model predicts both direct and cross damping coefficients whereas the Full-Sommerfeld model predicts that there are only direct damping coefficients.

Without any damping coefficients from the full numerical simulation, the damping coefficients that will be used in our model shall come from the Full-Sommerfeld model. This of course introduces some error to the results, since compressibility effects are not accounted for, but it is nonetheless, the best available option. Also, simple tests showed that the bearings performance trends are relatively insensitive to the damping models and mostly depend on the stiffness models used.

2.4.4 External Couette Flow Damping

Since the distance between the journal and the aft plate is relatively small, the magnitude of possible Couette flow damping was computed and compared to the damping due to hydrodynamics. Figure (2-7) shows the area over which Couette flow was assumed to exist:

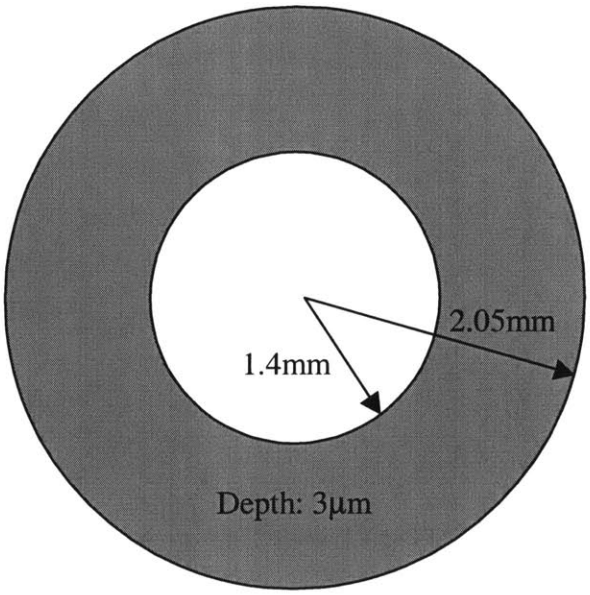

Figure 2-7: Surface over which Couette flow damping shall be calculated

The variation of velocity for Couette flow[18] is as follows:

$$u = \frac{u_o y}{d} \tag{2-46}$$

where u is the velocity of the flow at any point in the profile, u_o is the relative velocity at which the surfaces are moving, y is the vertical location in the profile and d is the separation between the two surfaces. Now the shear stress is a function of the slope of the profile and the coefficient of viscosity and is given by:

$$\tau = \mu \frac{\partial u}{\partial y} \tag{2-47}$$

Manipulating the two above equations, and using the fact that the shear stress is equal to the shear force per unit area, the following result is obtained:

$$F_{shear} = \left[\mu \frac{A_{wet}}{d} \right] u_o = b_{xx} u_o = b_{zz} u_o \tag{2-48}$$

Evaluating the bracketed expression determines the value of the Couette flow damping. It is then converted to the appropriate non-dimensional form using Eq. (2-49), which arises from (Eq 2-3, 2-6, and 2-12):

$$\overline{B}_{ii} = \frac{\psi^3}{12\mu L} b_{ii} \tag{2-49}$$

For the micro-bearing rig, the value of the Couette flow non-dimensional damping coefficient turns out to be 4.81×10^{-5} whereas the value of the damping coefficients predicted by the Full-Sommerfeld model at an eccentricity ratio of zero is 6×10^{-3}. The Couette flow damping coefficient is approximately two orders of magnitude smaller than the damping predicted by the Full-Sommerfeld model and as a result can be considered negligible. However, there could be other forms of unaccounted external damping, such as Coulomb damping. Examining these possibilities, however, goes beyond the scope of this thesis.

2.5 Solution Techniques

In operating the bearing rig, the only parameters that can be regulated by the user are the low pressure plenum pressure, the high pressure plenum pressure, and the turbine main air pressure; and the only variable which is of interest to the user is $\overline{\Omega}$. In this section we will show how to determine the value of $\overline{\Omega}$ based on the values of P_{PH}, P_{PL}, and P_{main}. Figure (2-8) schematically depicts the procedure that will be followed.

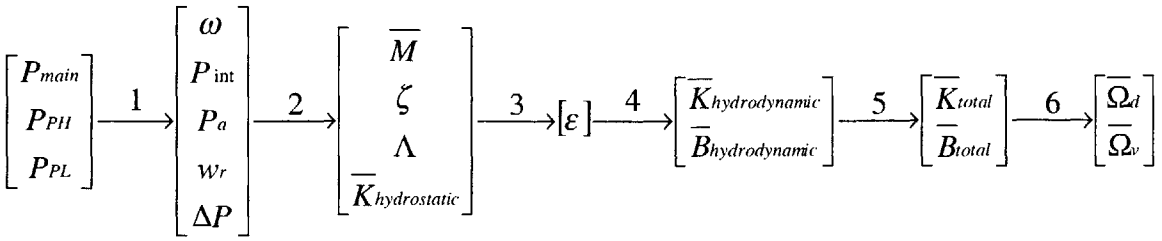

Figure 2-8: Functional dependence of variables

Step 1: Determination of ω, P_{int}, P_a, ΔP, and w_r

The angular speed of the rotor is a function of the main turbine air pressure P_{main}. The inverted functional relationship was predicted using MISES (a 2-D turbomachinery code developed by Professor Mark Drela) and is shown in Eq (2-50), and Figure (2-9).[14]

$$P_{main} = P_{atm}\left[\left(\frac{\omega r}{500}\right)0.956818 + \left(\frac{\omega r}{500}\right)^2 0.82273 + 1\right] \tag{2-50}$$

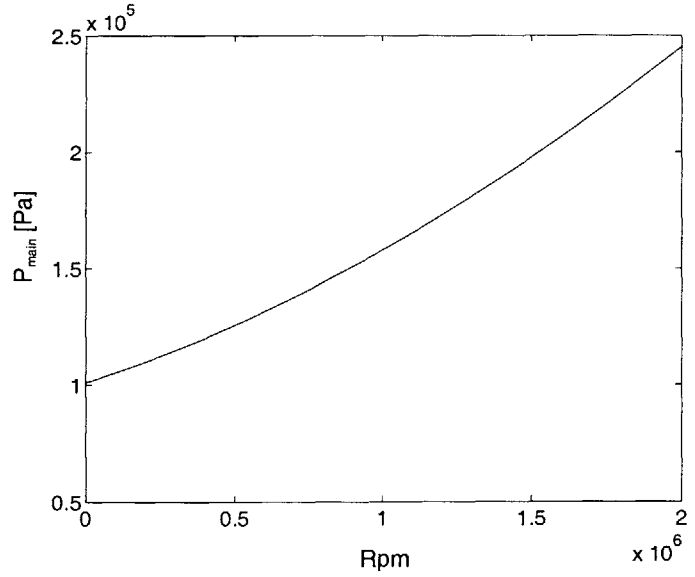

Figure 2-9: Rotor rpm vs. main turbine air pressure

The pressure after the air has flowed through the turbine blades is atmospheric and MISES predicts that the pressure between the stator and rotor blades should be the average of P_{main} and P_{atm}:[14]

$$P_{int} = \frac{P_{main} + P_{atm}}{2} \tag{2-51}$$

P_a, which was introduced earlier, is the ambient pressure, and is set to be the weighted average of all the pressures in the journal-bearing gap. A linear pressure distribution between the interrow pressure and the plena pressures is assumed and the ratio of the areas of the plena is 2:1:

$$P_a = \frac{P_{int}}{2} + \frac{P_{PH}}{3} + \frac{P_{PL}}{6} \tag{2-52}$$

The net load force experienced by the rotor is computed by computing the average pressures acting on each section of the journal and by multiplying these pressures by the appropriate areas:

$$W_r = \left(\frac{P_{int} + P_{PH}}{2} \right) A_h - \left(\frac{P_{int} + P_{PL}}{2} \right) A_l \tag{2-53}$$

where $A_h = A_l = (1/3)2\pi rL = 1.07 \times 10^{-6} m^2$

Since there are two plena, the pressure in the aft side of the bearing is not uniform. As a result, the pressure difference across the rotor is also computed as a weighted average of the pressure differences:

$$\Delta P = \frac{2(P_{PH} - P_{int})}{3} + \frac{(P_{PL} - P_{int})}{3} \tag{2-54}$$

Step 2: Determination of $\overline{M}$, ζ, Λ, and the Hydrostatic Stiffness

The mass parameter is computed using Eq. (2-8). The load parameter is computed using Eq. (2-9). The bearing number is computed using Eq. (2-7). And the hydrostatic stiffness coefficient is predicted using Eq. (2-34, 2-35, and 2-37).

Step 3: Determination of the Eccentricity Ratio

When examining the general case of hybrid operation, the stiffness' $\overline{K}_{ij}$ are composed of hydrostatic and hydrodynamic stiffness'. More specifically:

$$\overline{K}_{xz} = \overline{K}_{xz\_hydrodynamic} \qquad \overline{K}_{zx} = \overline{K}_{zx\_hydrodynamic} \tag{2-55}$$

$$\overline{K}_{xx} = \overline{K}_{xx\_hydrodynamic} + \overline{K}_{xx\_hydrostatic} \qquad \overline{K}_{zz} = \overline{K}_{zz\_hydrodynamic} + \overline{K}_{zz\_hydrostatic} \tag{2-56}$$

The value of the hydrostatic stiffness' has already been determined. Also, since the bearing number is known, the value of the hydrodynamic stiffness' is a known function of the eccentricity ratio (based on the results of the full numerical simulation). As a result, the total stiffness' of the system are also known functions of the eccentricity ratio.

In order to determine the actual eccentricity ratio, we first realize that when $\overline{K}$ is multiplied by Λ, the following relationship arises:

$$\Lambda\overline{K}_{ij} = \frac{\partial\zeta_i}{\partial\varepsilon_j} \tag{2-57}$$

The product of $\overline{K}_{ij}$, and Λ expresses the rate of change of the load parameter with respect to the eccentricity ratio. We then proceed by supposing that the externally applied load is no longer applied in a direction parallel to the x-axis but is applied in such a direction so that the displacement of the rotor is in only in the x-direction (i.e. ε_z = 0). Representing it in non-dimensional form by two components: ζ_x and ζ_z in the x and z directions respectively, Eq. (2-58) results:

$$\begin{pmatrix} \partial\zeta_x \\ \partial\zeta_z \end{pmatrix} = \begin{pmatrix} \Lambda\overline{K}_{xx} & \Lambda\overline{K}_{xz} \\ \Lambda\overline{K}_{zx} & \Lambda\overline{K}_{zz} \end{pmatrix} \begin{pmatrix} \partial\varepsilon_x \\ \partial\varepsilon_z \end{pmatrix} \tag{2-58}$$

However, since $\varepsilon_z = 0$ and also $\partial\varepsilon_z = 0$, Eq. (2-58) when integrated, reduces to two simpler equations:

$$\zeta_x = \int_0^{\varepsilon} \Lambda\overline{K}_{xx} d\varepsilon_x \qquad \zeta_z = \int_0^{\varepsilon} \Lambda\overline{K}_{zx} d\varepsilon_x \tag{2-59}$$

Adding the two load parameter components, the following resultant load is obtained:

$$\zeta = \sqrt{\zeta_x^2 + \zeta_z^2} \tag{2-60}$$

In Eq. (2-60), the load parameter is a function of the eccentricity ratio. But the actual value of the load parameter has already been computed. By iterating over the upper bound of the integrals in Eq. (2-59), we match the known load parameter with the one determined by Eq. (2-59 & 60) and thus determine the eccentricity ratio.

Step 4: Determination of the Hydrodynamic Stiffness and Damping

Given the eccentricity ratio and the bearing number, the hydrodynamic stiffness coefficients are computed using the results from the full numerical simulation. Also the hydrodynamic damping coefficients are computed using the Full-Sommerfeld model.

Step 5: Determination of the Total Stiffness

The total stiffness coefficients are obtained by adding the hydrostatic direct stiffness coefficients to the hydrodynamic stiffness coefficients, as was already shown in Step 3.

Step 6: Determination of $\overline{\Omega}$

All the required information is inserted into Eq. (2-16) and the values of $\overline{\Omega}$ are determined by finding the eigenvalues of the matrix A.

2.5.1 Determination of Stability Boundaries

Instead of looking at the value of $\overline{\Omega}$ only at specific operating points, it is of great value to be able to draw stability boundaries that define where the transition from stable to unstable operation occurs, and how different loading schedules change the stability characteristics of the rig.

2.5.1.1 Hydrodynamic Stability Boundaries

As has been mentioned in earlier sections, purely hydrodynamic operation is not possible using our bearing rig. However, we will examine it anyway, so as to get a physical understanding of its characteristics.

The first two steps shown in the schematic in Figure (2-7) are skipped and the value of $\overline{M}$ is set to a certain constant, based on the geometry of the bearing. Also, the hydrostatic stiffness coefficient is set to zero. A small bearing number is chosen and Steps 2-6 are iterated over increasing values of the load parameter until the value of $\overline{\Omega}_I$ switches from positive to negative, indicating that the bearing has transitioned from unstable to stable operation. This procedure is repeated for increasing Λ until the design speed is reached. Every time $\overline{\Omega}_I$ switches from positive to negative, the values of the load parameter, the bearing number and the whirling frequency ratio are recorded. Finally, the results are plotted on the ζ-Λ plane and the critical speed ratio vs eccentricity ratio plane. The second plot is a conventional way of plotting stability boundaries and represents the ratio of the speed to the whirling frequency as a function of the eccentricity ratio when operating neutrally stable.

2.5.1.2 *Hydrostatic Stability Boundaries*

Predominantly hydrostatic operation is possible using our bearing rig and the following procedure is used to determine hydrostatic stability boundaries. The plena pressures are set to the same value so that no loading is introduced. A small plena pressure is chosen and Steps 1-6 are iterated over increasing main turbine air pressure until the value of $\overline{\Omega}_l$ switches from negative to positive, indicating that the bearing has transitioned from stable to unstable operation. This procedure is repeated for increasing plena pressures. Every time $\overline{\Omega}_l$ switches from negative to positive, the values of the bearing number, the plena pressures, and the whirling frequency ratio are recorded. Finally, the results are plotted on the bearing number vs plena pressure plane and the critical speed ratio vs the eccentricity ratio plane.

2.6 Summary

In the first part of this chapter we showed how to determine whether the bearing could spin stably, and the value of its whirling frequency, based on the stiffness and damping coefficients, the mass parameter and the bearing number. Realizing that the user of the rig can only manipulate the plena pressures and the main turbine air pressure, we then showed how to determine the same stability parameters by using only these three later variables. Finally, we demonstrated how to draw hydrodynamic and hydrostatic stability boundaries whose purpose is to give us a more intuitive understanding of gas bearing operation.

CHAPTER 3

RESULTS AND DISCUSSION

In this chapter, we first validate our model using the Half and Full-Sommerfeld model coefficients by predicting hydrodynamic stability boundaries and comparing with those found in the bearing literature. Then a hydrodynamic and hydrostatic stability boundary is determined using the coefficients from the models that were suggested in Chapter 2. Finally, several hybrid pressure schedules are examined in search of a viable path to full speed operation.

3.1 Hydrodynamic Stability Boundaries

3.1.1 Model Validation

In order to validate our model, a hydrodynamic stability boundary is constructed using the Half-Sommerfeld model coefficients (Figure 3-1), based on the procedure described in Section 2.5.1.1.

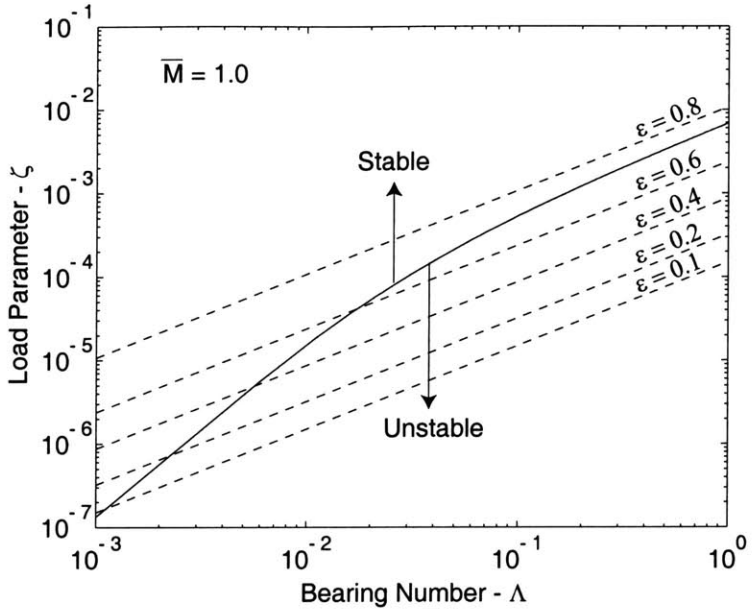

Figure 3-1: Hydrodynamic stability boundary, on the ζ-Λ plane, based on the Half-Sommerfeld model coefficients.

As expected, for a given bearing number, the bearing switches from unstable to stable operation as the eccentricity ratio is increased. Furthermore, at low bearing numbers, the bearing requires small eccentricity ratios to run stable but as the bearing number is increased, larger eccentricity ratios are required. An interesting fact is that as the bearing number is increased, the stability boundary asymptotes to an eccentricity ratio of approximately 0.76. This is one of the characteristics of the Half-Sommerfeld model and is one form of validation of our model.

The stability boundary can also be seen plotted on the critical speed ratio vs eccentricity ratio plane:

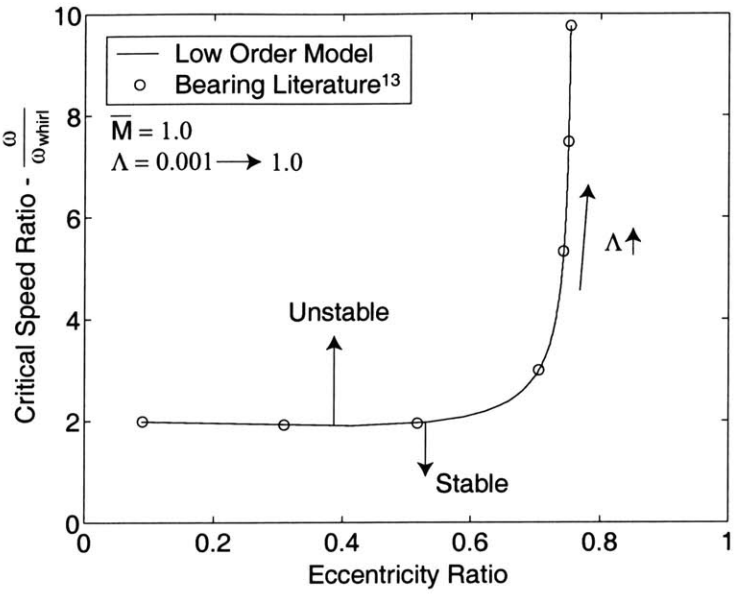

Figure 3-2: Hydrodynamic stability boundary, on the critical speed ratio vs eccentricity ratio plane, based on the half Sommerfeld coefficients. Sumperimposed on the stability boundary is a set of data points obtained from the bearing literature.[16]

The most interesting feature of the plot is that at eccentricity ratios below 0.6 the stability boundary rests at an approximately constant value of 2. This is known as *half-frequency* whirl and is referred to very often in the bearing literature. It implies that the journal has to be whirling at a frequency greater than half of its spinning frequency, in order to be stable. After an eccentricity ratio of approximately 0.76, the plot goes to infinity implying that the journal can be whirling at any fraction of the spinning frequency and still be stable. Superimposed on the plot are data points from the bearing literature, and as can be seen the model's results seem to be in perfect agreement with the literature.[16]

The Full-Sommerfeld model was also used to determine a stability boundary but, as expected, stable operation could not be achieved, even when very large loads were applied to the bearing.

3.1.2 Hydrodyanmic Stability Boundary

Having validated our model, using the Half and Full-Sommerfeld model coefficients, hydrodynamic stability boundaries using the full numerical simulation stiffness coefficients and the Full-Sommerfeld damping coefficients were constructed. The boundaries were drawn for mass parameters of 0.4, 0.9, and 2.0 and compared to the ones produced by the full numerical simulation. The reason why the boundaries were drawn for three different mass parameters, is that as the bearing number is increased the value of the mass parameter is expected to also increase due to the changing value of the ambient pressure and rotor radius. The mass parameters are expected to start at values slightly above 0.4 and end, at the design speed, at values slightly below 2.0. Figure (3-3, and 3-4) depict the results.

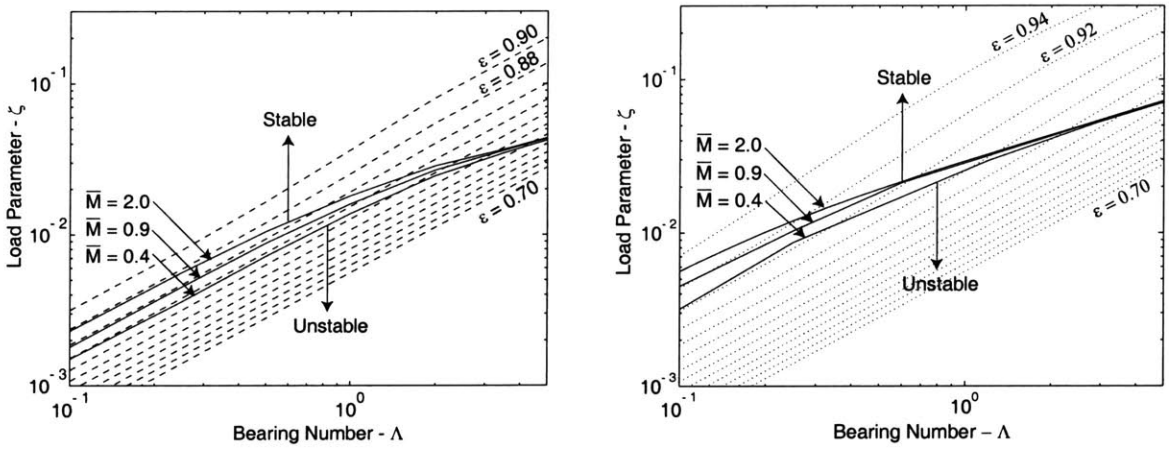

Figure 3-3: Hydrodynamic stability boundaries, on the ζ-Λ plane, for $\overline{M}$ = 0.4, 0.9, and 2.0. (a) Based on the low order model and (b) based on the full numerical simualtion.[15]

As can be seen the two models predict similar trends and only differ in that the full numerical simulation shows boundaries lying at slightly higher eccentricity ratios than the low order model dose. However, the deviation between the two models is acceptable since the purpose of the low order model is to only indicate trends in the behavior of the bearing.

Returning to the figures, several things can be observed: First, as the bearing number is increased, larger loads are required for the bearing to stay stable. This trend is similar to the results of the Half-Sommerfeld model. Second, as the bearing number is decreased the stability boundaries asymptote to constant eccentricities. This implies that even at small speeds, the bearing has to be operating at relatively large eccentricity ratios. This is different from the Half-Sommerfeld model where the stability boundaries go to an eccentricity ratio of zero as the bearing number is decreased. This result is also expected to cause a very large problem during startup, specifically at zero speed, since it will be impossible to load the bearing ever so slightly so as to achieve a finite eccentricity. Third, as the bearing number is increased, the eccentricity ratio of the stability boundaries decreases. This effect is due to compressibility effects and makes hydrodynamic operation look better as the speed is increased. Fourth, as the mass parameter is increased, the load parameter required to run stable for a given bearing number is increased. Along with the increase in the load parameter, there is also an increase in the eccentricity ratio, which leads to the conclusion that lower mass parameters are better. Remembering that the mass parameter depends on the ratio of the clearance to the radius of the journal, raised to the fifth power, it is realized that the performance of the bearing could be improved dramatically if the clearance was changed by only a very small fraction. This decrease in clearance (since the radius of the rotor is set by the overall system design), has been pursued, but the micro-fabrication techniques currently available are not able to do any better than twelve micro-meters, for the given length of the journal. Finally, as the bearing number is increased, the stability boundaries seem to be relatively insensitive to the mass parameter. This can be seen in the plot, where all the boundaries seem to collapse onto a single line at the higher bearing numbers. This leads to the conclusion that, if hydrodynamics are to be used only at high speeds, decreasing the mass parameter is not as important.

The plot shown in Figure (3-4) depicts the same stability boundaries as the ones in the previous plot, but the axes are now the critical speed ratio vs the eccentricity ratio:

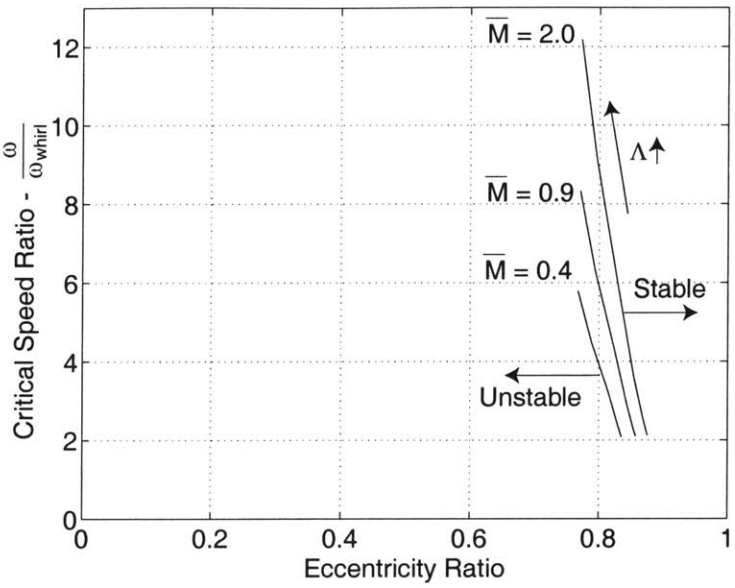

Figure 3-4: Hydrodynamic stability boundaries, on the critical speed ratio vs eccentricity ratio plane, for $\overline{M}$ = 0.4, 0.9, and 2.0.

Plotting the stability boundaries on these axes, also reveals several facts: First, at a bearing number of zero, the stability boundary shows that the critical whirling frequency is half of the spinning frequency. This result was also obtained for the Half-Sommerfeld model, for a range of low bearing numbers – where the eccentricity ratio was below 0.6. Second, as the bearing number is increased, the critical whirling frequency is expected to become a smaller fraction of the spinning frequency. Finally, as was observed in the previous plot, lower mass parameters cause the stability boundaries to lie at lower eccentricity ratios.

Having developed some basic physical insight in hydrodynamic operation, it is important to understand, as was mentioned earlier, that purely hydrodynamic operation is not possible in the current setup of the rig, because side loading will always introduce some amount of hydrostatics. This implies that these stability boundaries should only be used to understand the physics of hydrodynamic operation and should not be used as actual stability boundary predictions.

3.2 Hydrostatic Stability Boundary

Following the procedure described in Section 2.5.1.2, hydrostatic stability boundaries were constructed and are depicted in Figures (3-5, and 3-6).

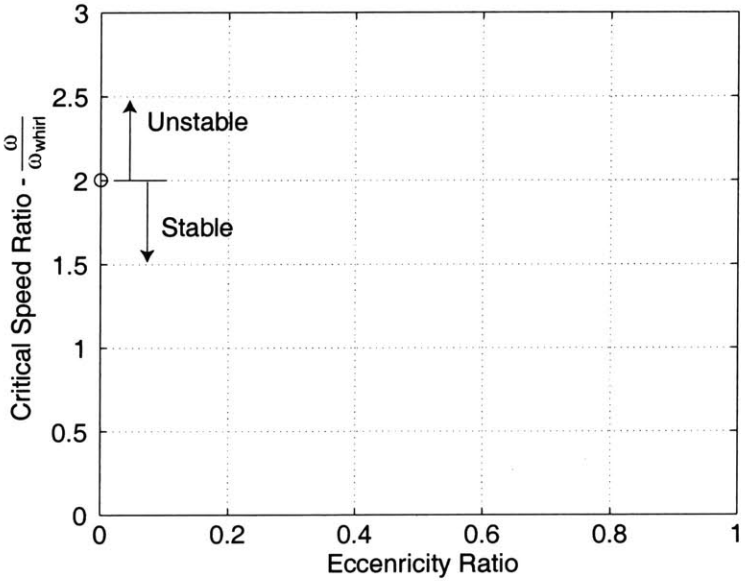

Figure 3-5: Hydrostatic stability boundary on the critical speed ratio vs. eccentricity ratio plane.

As can be seen in Figure (3-5), all the operating points lie on the critical speed ratio axis, since the eccentricity ratio at all times is zero. The interesting feature to notice, however, is that independent of the plena pressures, in order for the bearing to be stable, its whirling frequency has to be greater than half of its spinning frequency. This stability boundary is a characteristic of hydrostatic operation.

Figure (3-6), shows the stability boundary on the bearing number vs. plena pressure plane:

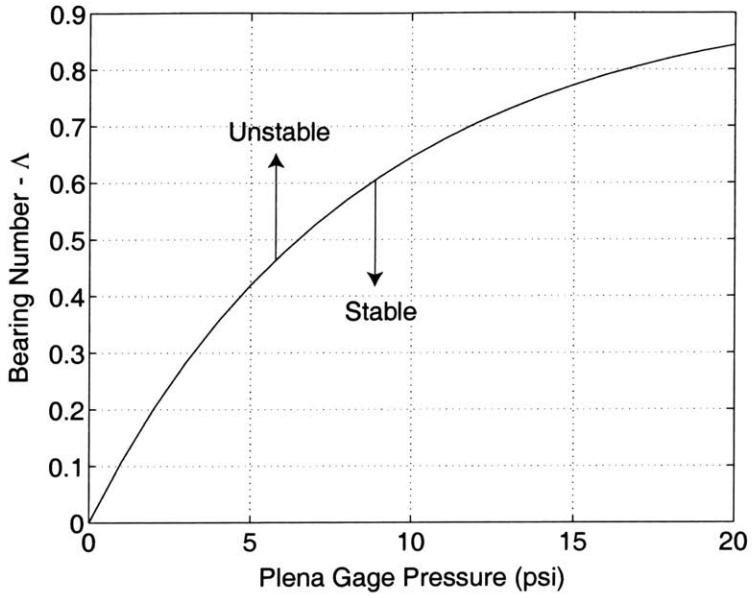

Figure 3-6: Hydrostatic stability boundary on the Λ vs plenum pressure plane.

As can be seen, the larger the pressure that is applied to the plena, the faster the journal can spin before going unstable. The reason is that as the plena pressures are increased, the hydrostatic direct stiffness coefficients are also increased, resulting in a stiffer bearing which can run stable up to higher speeds. Another important feature, is that as the plena pressures are increased, the stability boundary starts decreasing slope indicating that at larger plena pressures, large plena pressure increases will only result in small increases in the maximum bearing number. Remembering that full speed operation is between a bearing number of 3 and 5, it is realized that, based on this model, purely hydrostatic operation would require an extremely large amount of external pressurization.

3.2.1 Effects of External Damping on Hydrostatic Stability Boundary

Experimental results, in both the macro rig and micro rig have shown that the bearing was able to operate hydrostatically at critical speed ratios that were significantly greater than 2. The only explanation that can be given to this observation is that there exists some unaccounted external damping, or that the *viscoelastic* behavior suggested by the Larson and Richardson paper has a substantial role in our micro-bearing. Figure (3-7) depicts the effect of additional external isotropic damping on the hydrostatic stability

boundary. The critical speed ratio vs. the amount of external damping having been plotted for a bearing operating at a tip speed of $85ms^{-1}$ (approximately 400,000rpm).

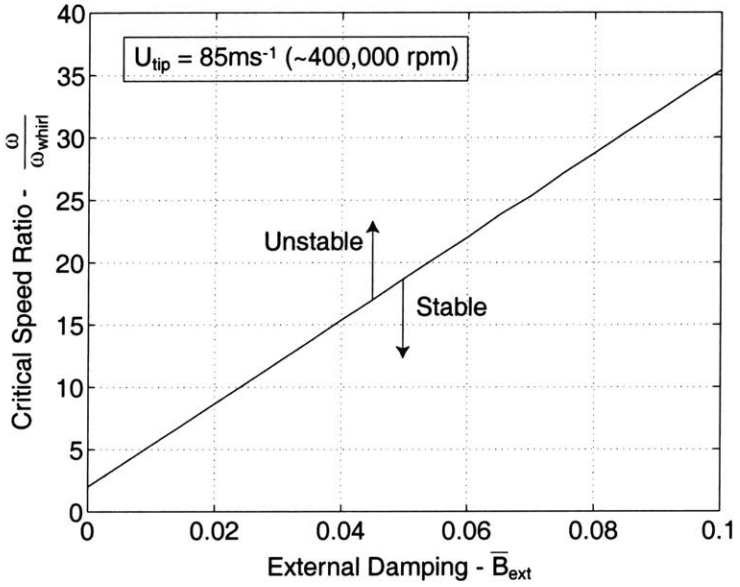

Figure 3-7: The effects of additional external damping on the hydrostatic stability boundary for a journal operating hydrostatically, at a tip speed of $85ms^{-1}$.

Remembering that the Full-Sommerfeld damping at an eccentricity ratio of zero is approximately 0.006, it is seen that an order of magnitude larger damping would be able to increase the critical speed ratio, of the hydrostatic stability boundary, by a factor of ten. This result confirms our initial belief that external damping could be causing the large critical speed ratios observed in the experiments.

3.3 Pressure Schedules

Section 2.5 explained how to determine the value of $\bar{\Omega}$ for one operating point (given the plena pressures and the main turbine air pressure). However, in order to examine possible paths that will lead us to full speed operation, it is necessary to actually define certain pressure schedules that will allow us to climb from zero speed to full speed and maintain stable operation at all times.

The structure of the pressure schedules that will be examined is such that the turbine main air pressure is the independent variable and the low and high pressure plena pressures are expressed as functions of it:

$$P_{PH\_gage} = P_{add} + \alpha(P_{main} - P_{atm}) = P_{add} + \alpha P_{main\_gage}$$
$$P_{PL\_gage} = P_{add} + \beta(P_{main} - P_{atm}) = P_{add} + \beta(P_{main\_gage}) \quad (3\text{-}1)$$

P_{add} is a constant pressure, which will be provided from some external source. It will be used to introduce hydrostatics to the system at low speeds, acting as a start-up assist, and will typically range from 0-5psi. α and β are constants representing what fraction of the turbine main air gage pressure is supplied to the high and low pressure plena, respectively. The value of α, and β will always be kept below 1 so as to make the whole system autonomous.

In examining any specific pressure schedule, the values of P_{add}, α, and β will be assigned a certain constant value and the procedure described in Section 2.6 will be iterated over P_{main} ranging from zero pressure to the pressure required for full speed. Several combinations of P_{add}, α, and β shall be examined so as to determine the best, and most feasible path to reach full speed. It is important to realize however, that this is a low order model and several assumptions have been made. The results are not to be interpreted as exact solutions to what the bearing is going to do for a given pressure schedule. Instead they are to be used as guides to understand what trends the operation of the bearing will have as a function of the three parameters described above. In the iteration, all the variables are tracked. For example the whirling frequency, the eccentricity ratio, the mass parameter, the bearing number and several others are all stored and can therefore be plotted once the code has run successfully.

First we will examine a purely hydrostatic pressure schedule where all of the main turbine air pressure is supplied to the plena:

$$P_{PH\_gage} = (P_{main} - P_{atm}) = P_{main\_gage}$$
$$P_{PL\_gage} = (P_{main} - P_{atm}) = P_{main\_gage}$$

In Figure (3-8), the turbine main air pressure and the inter-row pressures have been plotted as functions of the spinning frequency of the journal. Superimposed on the plot is a line representing the pressure that is required to be applied to the plena in order for the bearing to spin stably. Finally, a line representing the ratio of the available pressure difference: P_{main}-P_{int} vs. the required pressure difference, is plotted:

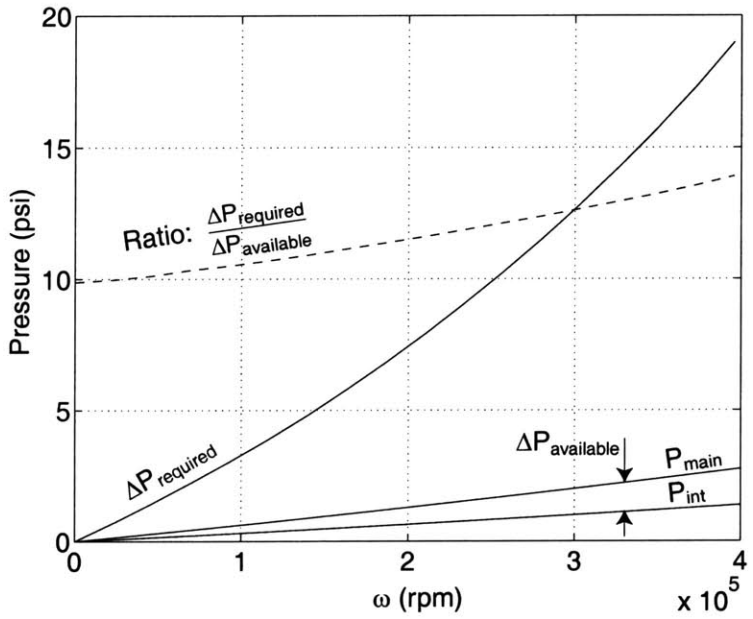

Figure 3-8: Hydrostatic pressure schedule for $\alpha = 1$, and $\beta = 1$. The main turbine air pressure and the inter-row pressure are plotted as functions of the rpm of the journal. The difference between the two – $\Delta P_{available}$ - represents the available pressure difference that could be used for the journal to perform hydrostatic operation autonomously. The $\Delta P_{required}$ line represents the amount of pressure difference that is required for the bearing to be stable at any certain spinning frequency. Finally the ratio line represents the ratio between $\Delta P_{required}$ and $\Delta P_{available}$.

The x-axis was chosen to be the spinning frequency of the journal instead of the bearing number because the ambient pressure for the $\Delta P_{required}$ line and the P_{main} and P_{int} lines was substantially different and as a result equal bearing numbers corresponded to different spinning frequencies. The plot clearly leads to the conclusion that, based on our model, autonomous hydrostatic operation is not feasible, because the required axial pressure difference is over ten times more than the available axial pressure difference. However, this result is in contradiction with experimental results, where the bearing was

spun up to 1.4 million rpm, based on what we believe to be purely autonomous hydrostatic operation (i.e. the pressures in the plena were equal and less than the main turbine air pressure). Possible reasons for this discrepancy are that a) there is some unaccounted external damping, b) the bearing is under the influence of viscoelastic effects, or c) the bearing was actually undergoing hydrodynamic operation.

Despite the fact that it appears as if our hydrostatic model may not be perfect, it is still acceptable to use it in order to predict the *trends* in the behavior of the bearing under different operating protocols. Also, even though the experiments showed that autonomous hydrostatic operation seems to be viable, the air mass flow through the journal-bearing gap was approximately 20-30% of the estimated total engine flow, which is unacceptably high. As a result, we will now examine several hydrodynamically dominated, hybrid pressure schedules, starting with a lightly loaded case and zero initial hydrostatic start-up assist:

$$P_{PH\_gauge} = 0.3(P_{main} - P_{atm}) = 0.3P_{main\_gauge}$$

$$P_{PL\_gauge} = 0$$

Figure (3-9) depicts the most important features of this pressure schedule:

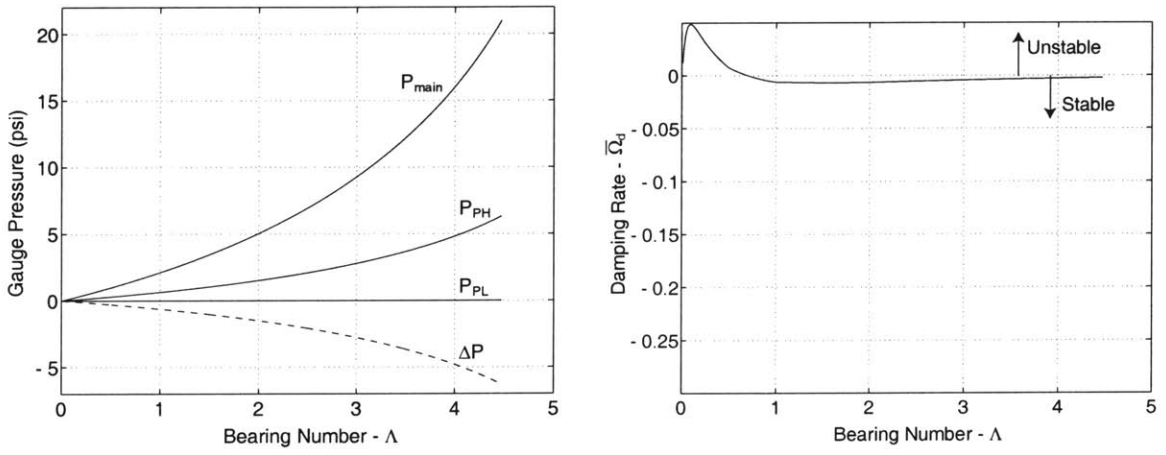

(a) (b)

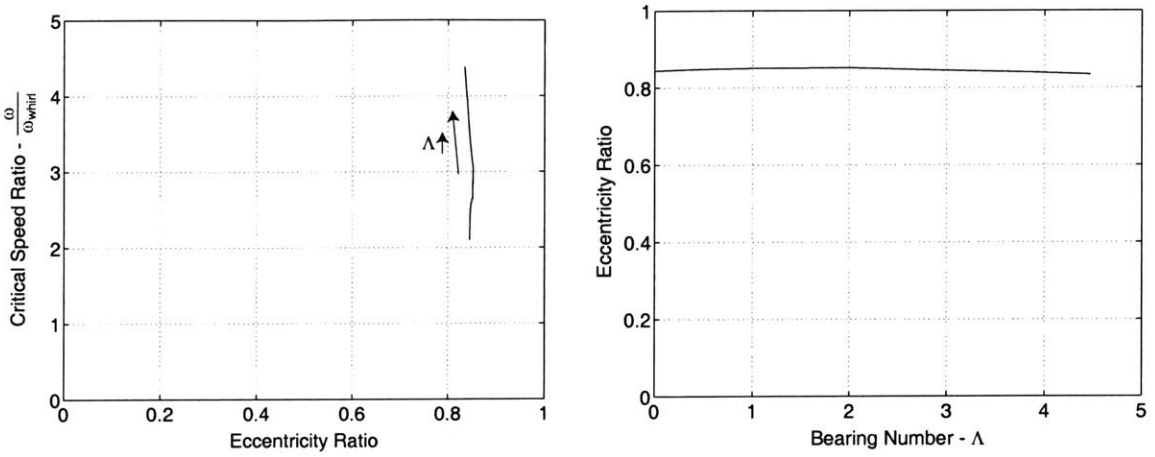

Figure 3-9: Pressure schedule results for $\alpha = 0.3$, and $P_{add} = 0$. (a) depicts the gauge pressures of the main turbine air, the high and low pressure plenum pressures and the axial pressure difference. (b) depicts the normalized damping of the bearing. (c) depicts the critical speed ratio as a function of the eccentricity ratio. (d) depicts the eccentricity ratio.

The first plot simply traces the gauge pressures of the main turbine air, the high pressure plenum, the low pressure plenum, and the axial pressure difference across the rotor. As can be seen, the low pressure plenum is vented and remains at a constant value of zero, whereas the high pressure plenum follows a path which is only a fraction of the main turbine air pressure. Also, as the speed is increased, the axial pressure difference, which started at zero, turns negative, representing the fact that the inter-row pressure is increasing at a faster rate then the average pressure of the two plena is. The second plot, which depicts the overall damping of the system, immediately reveals that the bearing is unstable at low speeds and turns stable as the speed is increased. The third plot shows how the critical speed ratio, starts at a value of 2, and increases with increasing speed due to the fact that the spinning frequency is increasing at a faster rate than the whirling frequency is. The fourth plot depicts the value of the eccentricity ratio, which is relatively constant, as a function of the bearing number. Initially its value is below 0.86 and based on Figure (3-3(a)), the fact that it is unstable at low bearing numbers was expected a priori.

Insisting on trying to make a hydrodynamically dominated bearing that will run at all bearing numbers, we move to moderate loading and leave the hydrostatic start-up assist unchanged, at a value of zero:

$$P_{PH\_gauge} = 0.4(P_{main} - P_{atm}) = 0.4P_{main\_gauge}$$

$$P_{PL\_gauge} = 0$$

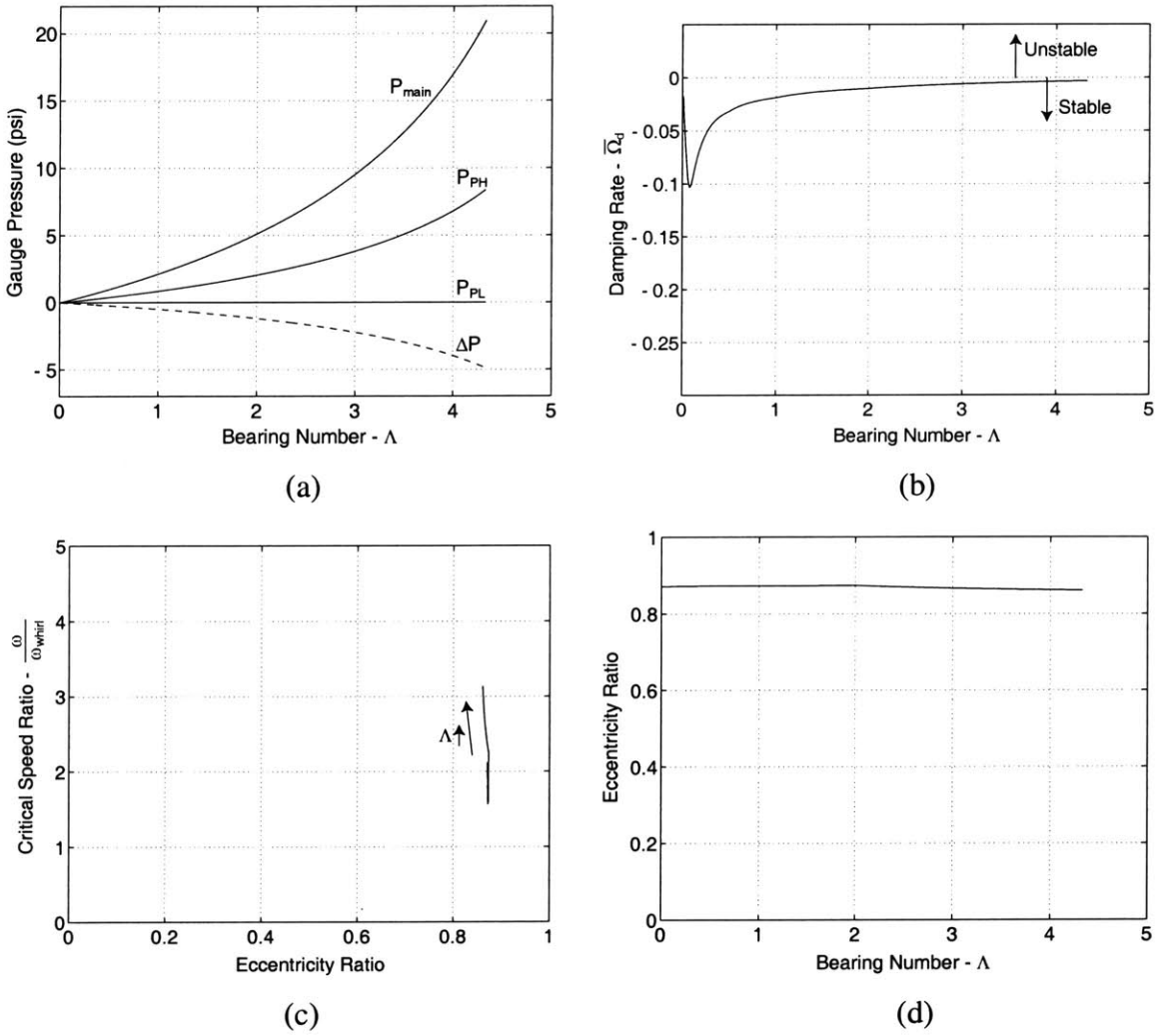

Figure 3-10: Pressure schedule results for $\alpha = 0.4$, and $P_{add} = 0$. (a) depicts the gauge pressures of the main turbine air, the high and low pressure plenum pressures and the axial pressure difference. (b) depicts the normalized damping of the bearing. (c) depicts the critical speed ratio as a function of the eccentricity ratio. (d) depicts the eccentricity ratio.

The increased load successfully pushed the journal to large enough eccentricities so as to assure stable operation at all speeds. The critical speed ratio, as expected, shows similar trends as those observed when α was 0.3. However an important problem arises. The bearing rig setup is not ideal and as a result, at infinitesimally small speeds, the

journal cannot be loaded so precisely so as to maintain an eccentricity ratio between 0.86 and 1.

The above problem is tackled by assigning a finite value to P_{add} so as to introduce hydrostatics to the system at low speeds. As a result we re-examine the previous moderately loaded case but this time we introduce a weak hydrostatic start-up assist.

$$P_{PH\_gauge} = 1psi + 0.4(P_{main} - P_{atm}) = 1psi + 0.4P_{main\_gauge}$$

$$P_{PL\_gauge} = 1psi$$

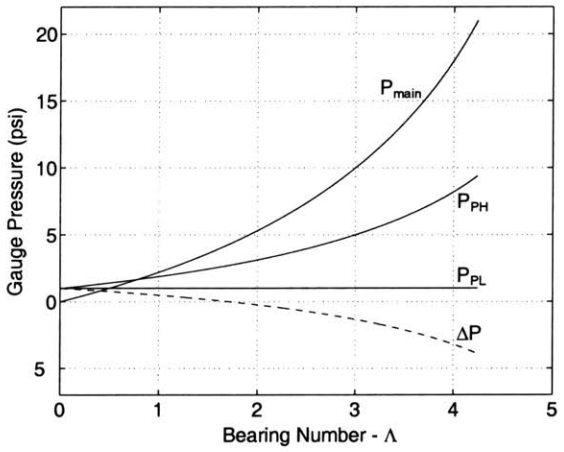

(a)

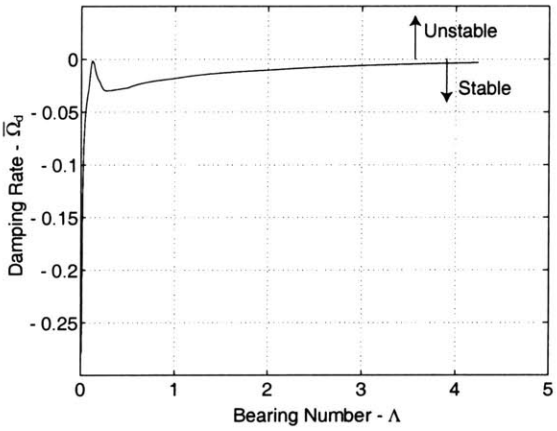

(b)

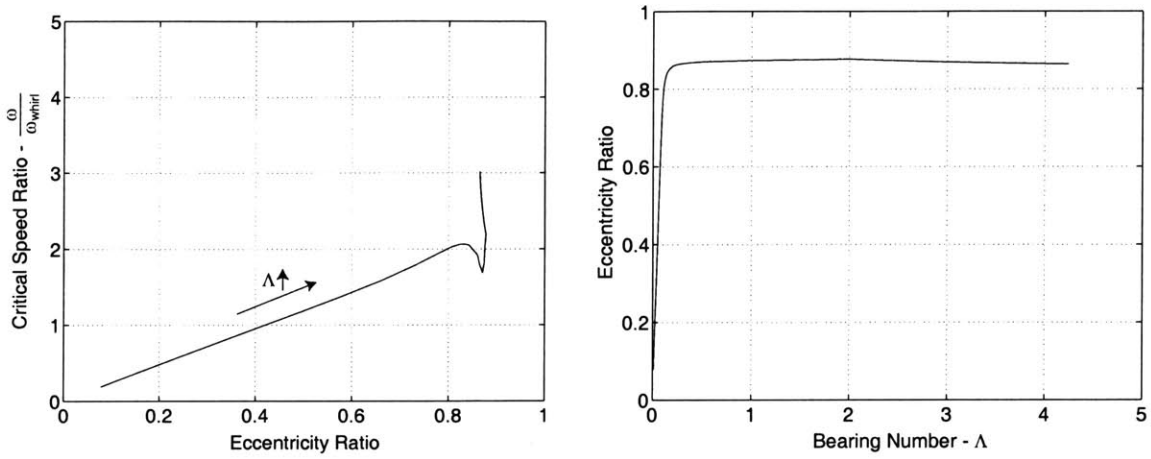

(c) (d)

Figure 3-11: Pressure schedule results for $\alpha = 0.4$, and $P_{add} = 1$. (a) depicts the gauge pressures of the main turbine air, the high and low pressure plenum pressures and the axial pressure difference. (b) depicts the normalized damping of the bearing. (c) depicts the critical speed ratio as a function of the eccentricity ratio. (d) depicts the eccentricity ratio.

The results show that the bearing was able to run stable at all the bearing numbers, but most importantly, it started at an eccentricity ratio of zero. As the bearing number was increased, so was the applied load, and as a result, the journal was moved back to the large eccentricity ratios it was operating at, in the previous example. The plot of the critical speed ratio initially is increasing at a constant rate. This is because at the low eccentricity ratios the bearing is operating pre-dominantly hydrostatically. As a result its whirling frequency is unaffected by the increasing eccentricity ratio, whereas its spinning frequency is increasing and therefore, the ratio of the two appears to be increasing. Just after an eccentricity ratio of 0.8, the bearing starts operating pre-dominantly hydrodynamically. As a result, the whirling frequency is seen to increase. The plot shows a decreasing ratio at first, because the whirling frequency is increasing at a faster rate than the spinning frequency is increasing. Once, the eccentricity ratio reaches its largest value, however, the rate at which the whirling frequency is increasing is smaller than the rate at which the spinning frequency is increasing. As a result, the plot shows an upward trend after the peak eccentricity ratio has been achieved. The important thing to conclude from Figure (3-11c), is that the transition from hydrostatic to hydrodynamic operation is observed as a change from a positive slope to a negative slope.

In order to examine the effect of increasing the hydrostatic start-up assist, the following pressure schedule was then examined:

$$P_{PH\_gauge} = 2psi + 0.4(P_{main} - P_{atm}) = 2psi + 0.4P_{main\_gauge}$$

$$P_{PL\_gauge} = 2psi$$

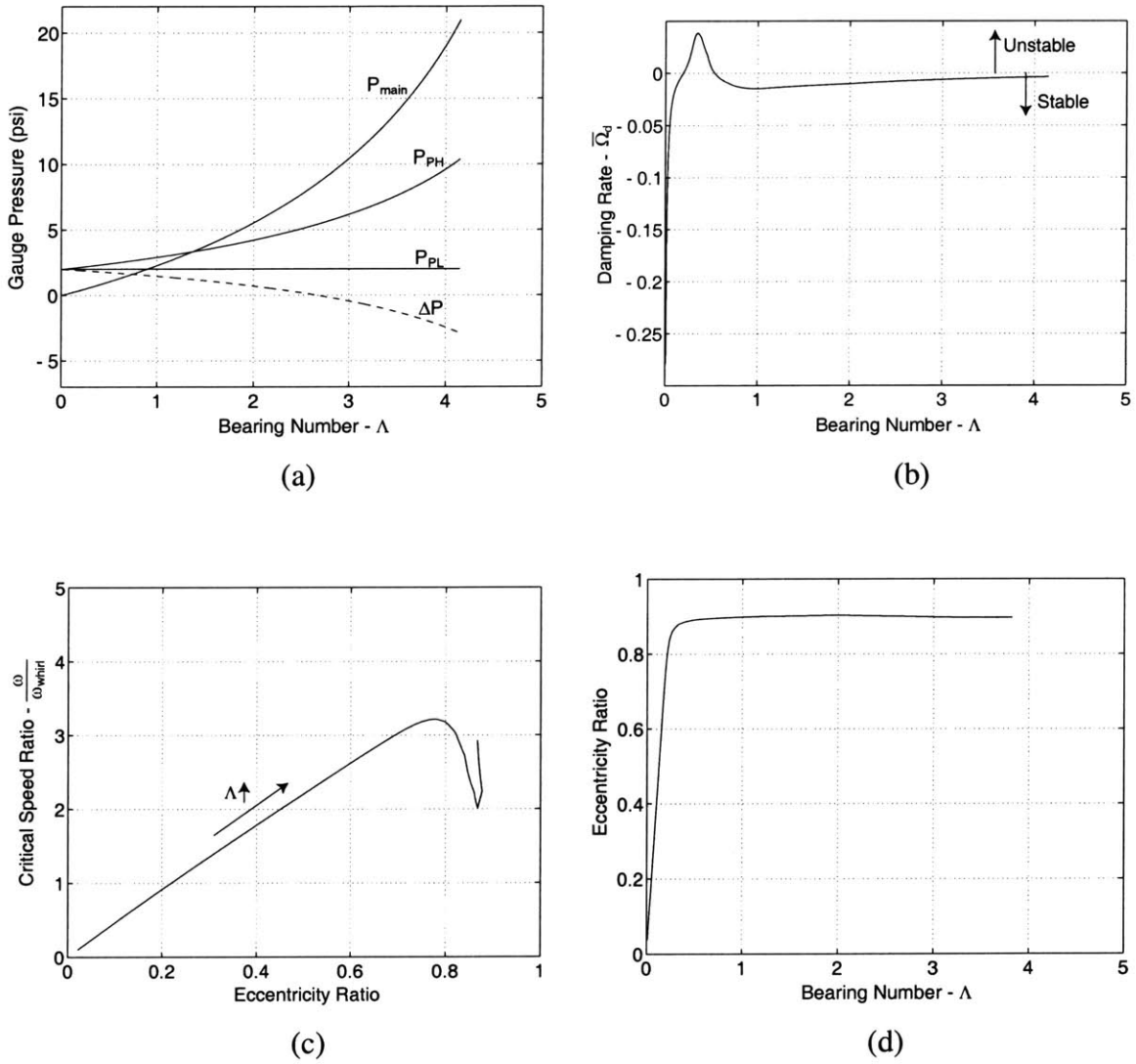

Figure 3-12: Pressure schedule results for α = 0.4, and P_{add} = 2. (a) depicts the gauge pressures of the main turbine air, the high and low pressure plenum pressures and the axial pressure difference. (b) depicts the normalized damping of the bearing. (c) depicts the critical speed ratio as a function of the eccentricity ratio. (d) depicts the eccentricity ratio.

As would intuitively be expected, the increased pressure in the plena make the eccentricity ratio change from a value of zero to its constant value, at a higher speed than

in the previous case. This is because the hydrostatics are now stronger, and it requires a larger load (and therefore higher bearing number) in order to push the journal to higher eccentricity ratios. However, in this case, the bearing starts stable – due to hydrostatics, but then becomes unstable, for a range of bearing numbers, until it finally becomes stable again. The reason why it is unstable during this range, is that the hydrostatic stiffness is not strong enough to keep it stable, but in the mean time is not allowing it to move to higher eccentricity ratios, so that the hydrodynamic stiffness' can kick in and maintain stability. This is a very important aspect of hybrid operation. If the of value of P_{add} was to remain at 2psi and the bearing had to be made stable, the value of α would have to be increased all the way to 0.7 so as to push the unstable range of bearing numbers into the stable regime. Physically, the higher loading would be causing the eccentricity ratio to increase faster and hydrodynamics to come into effect at a lower bearing number, before the bearing had a chance to go unstable.

Overall, it seems that hydrodynamic operation is good at higher bearing numbers and hydrostatic operation is good at lower bearing numbers. Full speed operation could ideally be achieved using only hydrodynamics but the bearing rig is not ideal and as a result hydrodynamics cannot be the only form of support of the bearing at low bearing numbers. Hydrostatic operation, on the other hand, should only be used to support the bearing at low bearing numbers, because based on this model, as the bearing numbers are increased, very large pressures are required to keep it stable. This is in disagreement with the experimental results. However, experiments do favor the conclusion that hydrostatics should only be used at low speeds, but for a different reason – the air mass flow rates required for high speed hydrostatic operation are too high. Moreover, it seems that the best solution is to perform hybrid operation, where the bearing is initially operating hydrostatically, and then transitions to hydrodynamic operation, as the speed is increased.

Hybrid operation has several good features associated with it, but it is also very hard to perform. Specifically, when transitioning from hydrostatic to hydrodynamic operation, as was explained earlier, it is very easy to either be applying to high a value of P_{add} or to low a value of α.

3.3.1 An Alternative Hybrid Path

The problem, in the previously suggested hybrid pressure schedules is in the transition from hydrostatic to hydrodynamic operation. One way around this problem, would be to remove the additional pressure from the plena once a small bearing number is reached, and essentially jump from one form of pressure schedule to another. For example, initially the pressure schedule shown in Figures (3-11) could be followed and at a bearing number of 0.1 the additional pressure would be shut off and all the curves would jump to the values depicted in Figures (3-9). This would remedy the problem but would also introduce another problem, which would be determining when to turn off the additional pressure. If the additional pressure is turned off too soon, two things could happen. Either the hydrodynamics could be too weak to support stable operation, or the non-idealities of the setup would not allow proper loading of the journal and would cause it to crash by either overloading it or by not loading it enough. If the additional pressure is turned off too late, the bearing might have already crashed because of the reasons why the previously mentioned hybrid operating protocols could crash.

3.4 Mode Bifurcation

In Chapter 2, it was mentioned that the solutions to Eq (2-16) could possibly give two whirling modes at any operating point. Until now, only the least damped one has been referred to, since it is expected to be the one which will be observed in the experiments. Despite this fact, in this section, we will examine what the second, highly-damped mode looks like. Figure (3-13), which is based entirely on hydrodynamic operation, depicts both the whirling ratios as a function of the eccentricity ratio at a constant bearing number of 4.5, and a constant mass parameter of 1.7:

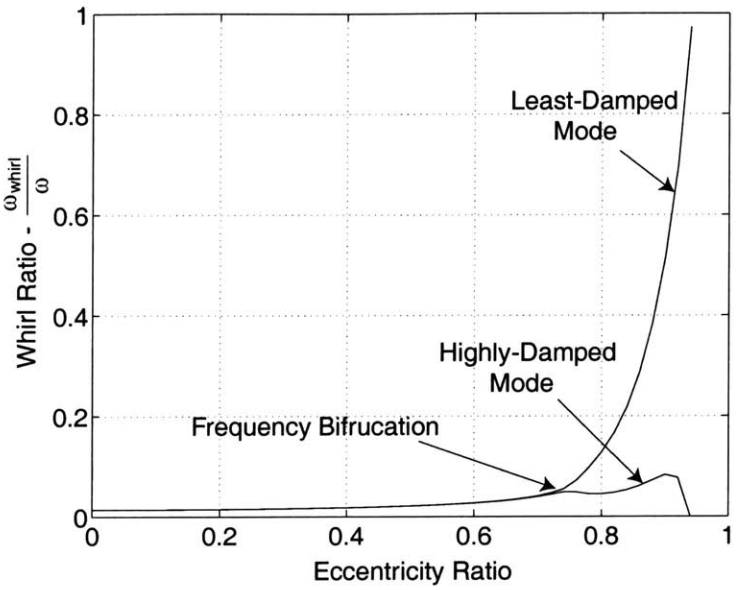

Figure 3-13: Frequency bifurcation. Both the whirling frequency ratios have been plotted as a function of the eccentricity ratio for a constant bearing number of 4.5 and a constant mass parameter of 1.7. The frequencies are identical at low eccentricity ratios but after an eccentricity ratio of 0.7, they bifrucate. The higher frequency of the two is the least damped one and therefore the one that is expected to be observed.

At low eccentricity ratios, both the frequencies have the same value. However, at an eccentricity ratio of approximately 0.7, a frequency bifurcation is observed. This suggests, that after eccentricity ratios of 0.7, two whirling modes will be present. It is important to realize, however, that only a small section of the plot, at high eccentricity ratios, represents possible, stable, operating points since only hydrodynamic effects are present. As a result, the actual bifurcation of the frequency, is just a mathematical abstraction, and could not be experienced under this type of protocol.

Figure (3-14), examines both the whirling frequencies for the pressure schedule depicted in Figure (3-11), and allows us to see if any such bifurcation could physically occur. In this case, the hydrostatics are allowing the lower eccentricity operating points to actually be stable. The frequencies are not normalized by the spinning frequency, as they previously were, because in this case when moving along the x-axis, the spinning frequency itself is changing. If the whirl ratios were plotted instead, the graph would be depicting both the changing spinning frequency and the changing whirling frequency, which would make the results unclear.

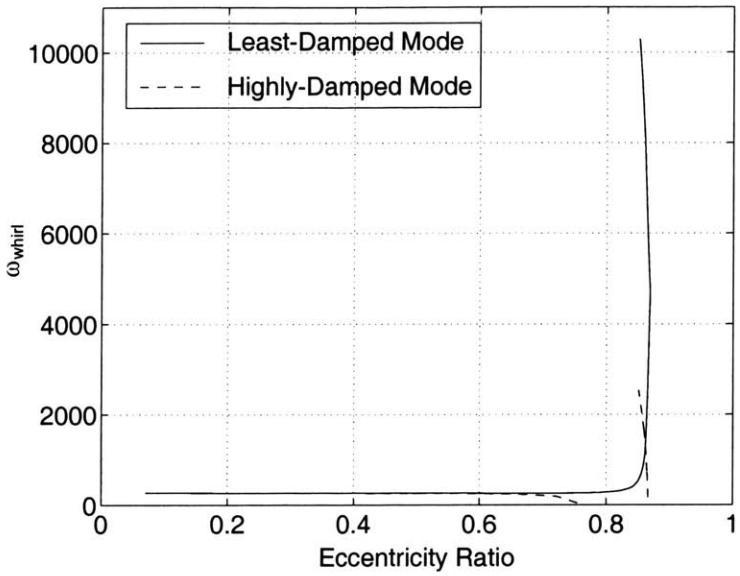

Figure 3-14: Frequency bifurcation for the pressure schedule where $\alpha = 0.4$ and $P_{add} = 1$psi. Both the whirling frequencies have been plotted as a function of the eccentricity ratio. A bifurcation occurs at an eccentricity ratio of approximately 0.7. At lower eccentricity ratios, the whirling frequencies are identical to the natural frequency that is associated with the hydrostatics that are present.

Remembering that this plot is substantially different from the one shown in the previous figure, in the fact that the bearing number is increasing along the curves, and whirling frequency is plotted instead of the whirling frequency ratio, several interesting things are noticed. A bifurcation is once again observed at an eccentricity ratio of approximately 0.7. As the eccentricity ratio is increased, the least damped frequency increases rapidly, whereas the highly-damped frequency drops to zero and then increases. At the lower eccentricities, the whirling frequencies are identical to the hydrostatic natural frequency. This is expected, however, since at those low eccentricities, the hydrostatic stiffness is the dominant one. However, at higher eccentricities, as the hydrodynamics are introduced, the least-damped frequency clearly depicts the stiffening of the bearing.

3.5 Operating the Rig

Since the results of this model should only be used to develop some physical insight in the operation of the bearing rig and not to predict exact pressure schedules that will

guarantee stable operation, the following list of possible problems and suggested solutions was created.

Finite α and $P_{add} = 0$:

Observation: The bearing cannot start

Reason: 1) The system is not ideal and the bearing is not getting loaded as expected at the very low speeds during start-up.

or 2) Assuming that is was getting loaded appropriately, α could be too low and therefore the eccentricity ratio would be too small to allow the bearing to perform stable hydrodynamic operation

or 3) Assuming that it was getting loaded appropriately, α could be too high and therefore the eccentricity ratio would be so large that the bearing would crash..

Remedy: 1) Add a finite value of P_{add} so as to make the eccentricity ratio zero right at strart-up.

Finite α and finite P_{add}:

Observation: The bearing cannot start

Reason: 1) The bearing actually has to start but goes unstable once the speed is increased even slightly, and the operator is observing that the bearing cannot start, whereas the bearing is starting but immediately crashes as the speed is increased.

Remedy: 1) Look at the remedy of the next observation

Observation: The bearing starts but starts going unstable ones the bearing number is increased

There are two separate cases for which this could be occurring:

A) The hydrodynamics, *alone*, at that bearing number can support stable operation.

Reason: 1) Assuming that transition to hydrodynamic operation is being pursued, the hydrostatics are not strong enough to support the bearing but in the mean time are not allowing the bearing to move

to high enough eccentricity ratios so that the hydrodynamic stiffness takes over.

Remedy: 1) a) Decrease the value of P_{add} so as to allow the bearing to transition to hydrodynamic operation.

b) Increase the value of α so as to cause the bearing to transition to hydrodynamic operation. This is *not recommended* however, since it might cause the bearing to crash at higher bearing numbers, by overloading it.

B) The hydrodynamics, *alone*, at that bearing number cannot support stable operation because the value of α is too low

Reason: 1) Assuming that transition to hydrodynamic operation has already been achieved, the value of α is too low to keep the journal at large enough eccentricity ratios so as to operate stably.

2) Assuming that transition to hydrodynamic operation is being pursued, the hydrostatics are not allowing the bearing to move to large enough eccentricities, but even if they were, the bearing would still go unstable since the hydrodynamics are not strong enough.

Remedy: 1) Increase the value of α so as to increase the eccentricity ratio.

2) Increase the value of α so as to convert the situation to case A and then deal with it accordingly.

Now, determining whether the bearing is operating under case A or case B, is impossible because the operator does not have enough information.

Moreover, the procedures described above can only be performed on a trial and error basis. They suggest possible solutions to problems and when one solution approach doesn't work, another one should be tried. An important piece of information, however, is the whirling frequency ratio. Based on this model, an increasing whirling frequency ratio (as the bearing number is increased) can be interpreted as an indication that the bearing has transitioned to hydrodynamic operation. The problem is that the other more sophisticated models that have been developed,[14] do not show such a dramatic increase in

the whirling frequency ratio. One possible reason for the difference is that the damping coefficients that were used in this model did not account for compressibility effects.

3.6 Summary

Several ways of operating the bearing were examined. As was shown, purely hydrodynamic operation is best for high speeds, even though in an ideal experiment it could work even at low speeds. Hydrostatic operation, on the other hand, is good for low speeds and assures that the bearing will be operating at low eccentricity ratios. However, at higher speeds, our model suggests that too much pressure is required for stable operation. Even though this is in disagreement with experimental findings, both favor the idea that hydrostatics should only be used at low speeds. As a result, it seems that hybrid operation, which relies on hydrostatics at low speeds, and hydrodynamics at high speeds, is the best way to operate the bearing.

In operating the bearing in a hybrid mode, however, a difficulty is encountered in transitioning between hydrostatic and hydrodynamic operation. The problem arises due to the fact that the hydrostatics may give out, but in the mean time may not allow the bearing to move to higher eccentricities for hydrodynamic effects to kick in.

Finally, the second, highly-damped, whirling frequency was examined and was found to be the same as the least-damped whirling frequency at low eccentricity ratios, but at eccentricity ratio of approximately 0.7 a bifurcation was observed. After the bifurcation, the least-damped frequency increased rapidly and the more heavily damped frequency decayed to zero and started rising again at higher eccentricities. However, since only the least-damped frequency is expected to be observed, only the trends of this frequency have been examined throughout this thesis.

CHAPTER 4

CONCLUSION

4.1 Summary of Work

In an effort to make the MIT micro-engine bearing operational, the model that was presented in this thesis, was developed. It relies on the stiffness coefficients from a full numerical simulation, and damping coefficients from the Full-Sommerfeld model. By applying Newton's second law of motion to the bearing, a governing equation for the bearing's performance was developed. Solutions to this equation were used to predict whether stable operation of the bearing was achievable and what its whirling frequency would be.

The model is based on several assumptions and its results are not very precise, especially at higher eccentricity ratios. However, the objectives of this thesis were successfully completed. The model was able to describe the expected behavioral trends of the bearing under hybrid operation based on prescribed plena pressure schedules.

The results suggested that hydrodynamics work best at high speeds and hydrostatics work best at low speeds. It was therefore concluded that the best way to operate the bearing is in a hybrid mode, where at low speeds the journal is supported by hydrostatics and at higher speeds it is supported by hydrodynamics. In transitioning between the two modes, however, it was discovered that it was possible to crash the bearing due to the interaction between the hydrostatics and the hydrodynamics. More specifically, the hydrostatics could be too weak to support stable operation but also too strong to let the journal move to higher eccentricity ratios, where the hydrodynamic stiffness' could take

effect. Nonetheless, the model showed that the transition was possible if the correct plena pressures were used.

In all the analysis, only the least-damped frequency was examined, because the highly-damped frequency is not expected to be observed (due to its higher damping). A brief examination of the second whirling frequency, showed that its value was identical to the least-damped frequency, at low eccentricity ratios. However, at higher eccentricity ratios, a bifurcation was noticed where the least-damped frequency started rapidly increasing, whereas the highly-damped frequency remained quite constant.

4.2 Where Can the Model be Improved?

The low order model can be improved in several ways. First, in the hydrodynamic analysis, the fluid film is treated as if it is de-coupled from the rotor's motion. This is not correct. However, the effect of this de-coupling is subtle at low eccentricity ratios and noticeable only at high eccentricity ratios. As a result, the low order model's predictions are reasonably accurate up to eccentricity ratios of 0.8 at which point the model could use some improvement. Also, a better hydrostatic model could be, such as the one suggested by Larson and Richardson[9] where the viscoelastic nature of the hydrostatic bearing is included in the analysis. Finally, a better damping model could be used, where the damping coefficients account for compressibility effects. A possible source for such coefficients is the model developed by Orr[6].

4.3 Overall Conclusion

The micro-bearing rig can exhibit stable operation, and successfully reach the design speed, if the appropriate pressure schedules are used. The best way this can be done, is in a hybrid mode where special attention should be given to the transition between hydrostatic and hydrodynamic operation.

BIBLIOGRAPHY

[1] A.H. Epstein, S.D Senturia, O. Al-Midani, G. Anathasuresh, A. Ayon, K. Breuer, K-S Chen, F.F. Ehrich, E. Esteve, L. Frechette, G. Gauba, R. Ghodssi, C. Groshenry, S. Jocobson, J.L. Kerrebrock, J.H. Lang, C-C Lin, A. London, J. Lopata, A. Mehra, J.O. Mur Miranda, S. Nagle, D.J. Orr, E. Piekos, M.A. Schmidt, G. Shirley, S.M. Spearing, C.S. Tan, Y-S Tzeng, I.A. Waitz, "Micro-Heat Engines, Gas Turbines, and Rocket Engines – The MIT Microengine Projet", *28th AIAA Fluid Dynamics and 4th AIAA Shear Flow Control Conference*, (June 1997).

[2] A.H. Epstein, S.D Senturia, G. Anathasuresh, A. Ayon, K.Breuer, K-S Chen, F.F. Ehrich, G. Gauba, R. Ghodssi, C. Groshenry, S. Jacobson, J.H. Lang, C-C Lin, A. Mehra, J.O. Mur Miranda, S. Nagle, D.J. Orr, E. Piekos, M.A. Schmidt, G.Shirley, S.M. Spearing, C.S. Tan, Y-S Tzeng, I.A. Waitz, "Power MEMS and Microengines", presented at *IEEE Transducers on Solid State Sensors and Actuators,* Chicago, IL, (June 1997).

[3] *The MIT Microengine Project,* 1998 Annual Technical Report, MIT Propretary, Cambridge, MA (1998).

[4] *Micro Gas Tubine Generators and Technology Foundations for Micro Heat Engines,* ARO Annual Presentation, MIT Proprietary, Cambridge, MA, (April 1999)

[5] K-S Chen, "Materials Characterization and Structural Design of Ceramic Micro Turbomachinery", Ph.D. Thesis, Department of Mechanical Engineering, MIT, Cambridge, MA, (Feb 1999)

[6] D.J. Orr "Macro-Scale Investigation of High Speed Gas Bearings for MEMS Devices", Ph.D. Thesis, Department of Aeronautics and Astronautics, MIT, Cambridge, MA, (1999)

[7] C.C. Lin, "Development of Microfabricated Turbine Driven Air Bearing Rig", Ph.D. Thesis, Department of Mechanical Engineering, MIT, Cambridge, MA, (1999)

[8] J.W. Lund, "Self Excited, Stationary Whirl Orbits of a Journal in a Sleeve Bearing", Ph.D. Thesis, Rensselaer Polytechnic Institute, Troy, NY, (1966)

[9] J.W. Lund, (1979): "Rotor-Bearing Dynamics", Lecture Notes. Technical University of Denmark, ISBN 83-04-00267-1

[10] J.W. Lund, (1987): Review of the Concept of Dynamic Coefficients for Fluid Film Journal Bearings. ASME Trans., J.Tribology, vol. 109, no.1, pp. 37-41

[11] R.H. Larson and H.H. Richardson, "A Preliminary Study of Whirl Instability for Pressurized Gas Bearings", *Journal of Basic Engineering,* (December 1962).

[12] H.H. Richardson, (1958): Static and Dynamic Characteristics of Compensated Gas Bearings. Trans. ASME, vol. 80, pp. 1503-1509

[13] H.S. Cheng and C.H.T. Pan, "Stability Analysis of Gas-Lubricated, Self-Acting, Plain, Cylindrical, Journal Bearings of Finite Length, Using Galerkin's Method", *Journal of Basic Engineering*, (March 1965).

[14] S. Jacobson, personal communiation

[15] E.S. Piekos, "Numerical Simulation of Gas Lubricated Journal Bearings for Microfabricated Machines", Ph.D. Thesis, Department of Aeronautics and Astronautics, MIT, Cambridge, MA, (1999)

[16] B.J. Hamrock: *Fundamentals of Fluid Film Lubrication*, McGraw-Hill Company, New York, 1994

[17] K.S. Breuer, personal communication

[18] J.D. Anderson, Jr.: *Fundamentals of Aerodynamics*, 2d ed., McGraw-Hill Book Company, New York, 1991